

Copyright

by

Michael Scott Worthington

2010

The Thesis Committee for Michael Scott Worthington
Certifies that this is the approved version of the following thesis:

**Design and Analysis of the Hobby-Eberly Telescope Dark Energy
Experiment Bridge**

APPROVED BY
SUPERVISING COMMITTEE:

Supervisor:

Steven P. Nichols

Joseph H. Beno

**Design and Analysis of the Hobby-Eberly Telescope Dark Energy
Experiment Bridge**

by

Michael Scott Worthington, B.S.

Thesis

Presented to the Faculty of the Graduate School of
The University of Texas at Austin
in Partial Fulfillment
of the Requirements
for the Degree of

Master of Science in Engineering

The University of Texas at Austin
May, 2010

This thesis is dedicated to my wife for her endless love, support
and encouragement.

I can only hope that I will instill the same level of importance of education in my two
daughters as I received from my parents, for which I am eternally grateful.

Acknowledgements

I express my sincere gratitude to all those that have contributed to my success in this endeavor. Above all, to my wife Jenny for her constant support and sacrifices she has made during the pursuit of this degree. I also want to express my appreciation to Dr. Steven Nichols and Dr. Joseph Beno for their time, technical expertise and assistance in the research and writing phases of this thesis. Finally, I would like to thank the following people at the Center for Electromechanics and McDonald Observatory for their contributions and guidance throughout the design process and my career:

Center for Electromechanics:

Richard Hayes	Tim Beets
Joey Zierer	Sarah Hinze
Ian Soukup	Brian South
Nick Mollison	Rex Jackson
Dr. Brian Murphy	Dave Prater

McDonald Observatory:

John Good
John Booth

May, 2010

Abstract

Design and Analysis of the Hobby-Eberly Telescope Dark Energy Experiment Bridge

by

Michael Scott Worthington, M.S.E.

The University of Texas at Austin, 2010

Supervisor: Steven P. Nichols

A large structural weldment has been designed to serve as the new star tracker bridge for the Dark Energy Experiment upgrade to the Hobby-Eberly Telescope at McDonald Observatory. The modeling approach, analysis techniques and design details will be of interest to designers of large structures where stiffness is the primary design driver. The design includes detailed structural analysis using finite element models to maximize natural frequency response and limit deflections and light obscuration. Considerable fabrication challenges are overcome to allow integration of precision hardware required for positioning the corrector optics to a precision of less than 5 microns along the 4-meter travel range. This thesis provides detailed descriptions of the bridge geometry, analysis results and challenging fabrication issues.

Table of Contents

List of Tables	ix
List of Figures	x
Nomenclature	xii
1. Overview	1
1.1. Introduction	2
1.2. Objective	4
1.3. Organization	4
2. Prior Art	6
2.1. Literature Review	6
2.2. HET Lessons Learned	9
3. Hobby-Eberly Telescope	13
3.1. Bridge Functions	14
3.2. Existing Constraints	20
3.3. HETDEX Constraints	22
3.4. Operation Parameters	29
4. Solid Modeling	33
4.1. Bridge Design	34
4.2. Key Features and Geometry	37
4.2.1. Main Bridge Sections	38
4.2.2. End Sections	43
4.2.3. Y-Drive Support Structure	46
5. Finite Element Analysis	48
5.1. Natural Frequency Analysis	51
5.1.1. Design Process	52
5.1.2. Final Results	53
5.2. Deflection Analysis	57
5.3. Stress Analysis	59
5.3.1. Stress Results	61

5.3.2. Buckling Results	63
6. Fabrication	66
6.1. Welding Specifications.....	67
6.2. Machining Details.....	68
7. Discussion.....	71
7.1. Summary and Conclusions	72
7.2. Contributions	73
7.3. Future Work.....	75
Appendix A: Modeling Simplifications.....	78
Appendix B: Finite Element Analysis Constraints	82
B.1. LX Bearing Arrangement.....	83
B.2. UX Bearing Arrangement	86
B.3. LHF Bearing Arrangement	88
Appendix C: Modeling Validation.....	90
References.....	93
Vita.....	96

List of Tables

Table 3.1: Travel comparison between HET and HETDEX	25
Table 3.2: Comparison of HETDEX and HET component masses.....	31
Table 5.1: Summary of FEA results	51
Table 5.2: Interpretation of possible buckling load factor (BLF) values.....	61
Table B.1: LX linear bearing loads per block.....	86
Table B.2: UX linear bearing loads per block	88
Table C.1: Model validation results comparing Simulation and Algor	91

List of Figures

Figure 1.1: Aerial view of the Hobby-Eberly Telescope at McDonald Observatory	3
Figure 2.1: Beam element diagram displaying the six groups of loads on a beam.....	9
Figure 3.1: Cutaway rendering of the Hobby-Eberly Telescope revealing the primary components	14
Figure 3.2: SolidWorks' screenshot of upper hex with full tracker and coordinate system displayed	15
Figure 3.3: Screenshot of the simplified HETDEX payload and hexapod actuator arrangement	16
Figure 3.4: FMS carriage mounted to the side of the bridge guiding an IFU bundle.....	18
Figure 3.5: Overhead view of the HET Y-axis roller screw mounted above the primary beam of the bridge	19
Figure 3.6: The nested hexapod actuators (not shown) attach to the upper and lower members of the carriage (highlighted in green) on the HET tracker	23
Figure 3.7: Photo of SALT tracker (top) & SolidWorks' screenshot of HETDEX tracker showing how the main bridge beams angle downwards from the upper hex	24
Figure 3.8: SALT bridge showing the location of the Y-screw outboard of the primary beam.....	27
Figure 3.9: HETDEX center pull Y-drive assembly (highlighted in light blue)	27
Figure 4.1: Current bridge with labels of main sections	36
Figure 4.2: Bridge design constructed completely from HSS members (top) and redesign optimizing obscuration utilizing bar, plate and HSS members (bottom)	37
Figure 4.3: Section views of the secondary beam, left, and the primary beam, right. Evident are the main linear bearing rails and ways (light blue), the FMS linear bearing rails and ways welded to the sides of the beams and the bumpstop mounts in the background.....	38
Figure 4.4: Upper bulkhead (blue) and mounting bracket (green) for the Y-drive, slew drive assembly and roller screw nut	42
Figure 4.5: LX bridge end with top plate shown semi-transparent to reveal the 'H' shaped LX cable handler bracket attachment point	43
Figure 4.6: Top view of the LX bridge end showing the roller screw, slew drive and tracking drive	44

Figure 4.8: Y-drive support structure extending from the UX bridge end	47
Figure 5.1: SolidWorks' Simulation mesh of the bridge with applied constraints shown (green arrows)	48
Figure 5.2: Comparison of the tracker bridge model (upper) to the beam model created for FEA	50
Figure 5.3: Overhead and side views of the first mode frequency response (units = mm, deformation scale = 125)	55
Figure 5.4: Overhead and side views of the second mode frequency response (units = mm, deformation scale = 125)	56
Figure 5.5: Side view of the third mode frequency response (units = mm, deformation scale = 55)	57
Figure 5.6: Bridge Z-axis deflection with the full payload resulting in maximum deflection of -2.257 mm (units = mm, deformation scale = 300)	59
Figure 5.7: Beam segment loading convention applied in SolidWorks Simulation	60
Figure 5.8: Results displaying the worst case stresses (units = MPa)	62
Figure 5.9: Plot showing each bridge beam in tension (red), compression (blue) or under no axial stress (green)	63
Figure 5.10: First buckling mode revealing the beam member most susceptible to buckling with a calculated buckling load factor of -7.61	64
Figure 6.1: Machined mounting surfaces (shown in blue) for the Y-drive assembly.....	70
Figure A.1: Section view comparison of the real Y-drive housing model (left) and the model created for the beam analysis (right).....	79
Figure B.1: End view of the LX end of the bridge showing the bearing arrangement and load paths where blue lines represent Z-axis loads, red lines are X-axis loads and yellow lines are Y-axis loads	84
Figure B.2: End view of the UX end of the bridge showing the bearing arrangement and load paths where blue lines represent Z-axis loads, red lines are X-axis loads and yellow lines (into the page) are Y-axis loads.....	87
Figure B.3: View of the secondary side of the bridge revealing the X-blocks on short rails mounted directly above the main Y-blocks	89

Nomenclature

TERM:	DEFINITION:	FIRST USE:
CAD	computer aided design	33
CCAS	center of curvature alignment sensor	13
CDR	critical design review	35
CEM	Center for Electromechanics	2
CFD	constant force drive	28
CG	center of gravity	23
DEX	Dark Energy Experiment	2
DOF	degree of freedom	4
FEA	finite element analysis	4
FMS	fiber management system	17
HET	Hobby-Eberly Telescope	1
HETDEX	Hobby-Eberly Telescope Dark Energy Experiment	3
HSS	hollow structural section	25
IFU	integral field unit	17
LHF	lower hexapod frame	17
LX	lower-X	19
MDO	McDonald Observatory	1
PFIP	prime focus instrument package	16
SALT	Southern African Large Telescope	10
UX	upper-X	19
VIRUS	visible IFU replicable unit spectrograph	17
WFC	wide field corrector	16

1. Overview

Numerous factors drive the design of structural components. Mass, volume, cost, material requirements and loading are a few parameters that may significantly impact the design. The component's function(s) and operating environment ultimately determines which parameters steer the design.

One structural component for the Hobby-Eberly Telescope (HET) at McDonald Observatory (MDO) is the tracker bridge. The bridge spans the upper hexagon structure and supports the corrector optics which captures light reflecting off of the primary mirror. Key design parameters are stiffness, characterized via natural frequency response, deflection from the mass of the payload, light obscuration and overall mass. These parameters were of equal importance during the initial design as during the major telescope upgrade. The key difference between designs is the significant increase in payload which the bridge supports.

This thesis details the design process of the bridge for the HET upgrade. An overview of the telescope and its functions is given to explain the driving constraints of the bridge design. Upon constructing the bridge in solid modeling software, the bridge is analyzed using finite element software. Final results of these analyses are presented, along with important fabrication considerations.

1.1. INTRODUCTION

The Hobby-Eberly Telescope, Figure 1.1, is the flagship telescope at The University of Texas' McDonald Observatory [1, 2]. The HET is located approximately 6600 feet above sea level on Mt. Fowlkes in the Davis Mountain Range in West Texas. It was created and is operated as a joint project with The Pennsylvania State University, Stanford University, Ludwig-Maximilians-Universität München, and Georg-August-Universität Göttingen [3]. The HET has been performing science operations since October of 1999 [3]. The primary mirror spans 78 square meters with an effective aperture of 9.2 meters, making HET the fourth largest optical telescope in the world¹ [4]. The telescope is optimized for spectroscopy, which is the process of decoding light from stars and galaxies to study their properties [5].

The HET is currently undergoing a major upgrade to study dark energy. The upgrade, termed the Dark Energy Experiment (DEX) [6-8], will conduct the largest survey of distant galaxies ever attempted. The goal of this survey is to measure the changing rate that the universe has been expanding over time due to dark energy. This knowledge will be paramount to astronomers in their understanding of dark energy and the effect that it has on the universe.

Beginning in late 2007, The University of Texas' Center for Electromechanics (CEM) began work on redesigning the tracker, drive systems and software controls for

¹ (1) Large Binocular Telescope, 11.8 m effective aperture; (2) Keck 1 & 2, 10.6 m each; (3) Great Canary Telescope, 10.4 m; (4, tie) HET and Southern African Large Telescope, 9.2 m [9]

the upgrade, referred to as HETDEX. Sections of the redesign that directly affect the bridge design are discussed in additional detail.



Figure 1.1: Aerial view of the Hobby-Eberly Telescope at McDonald Observatory

Source: Marty Harris, McDonald Observatory [2]

Given the magnitude of the HETDEX upgrade, CEM utilized twelve engineers and two mechanical designers during the various phases of the project. While subsystems are assigned to each engineer, the design work of each section is highly dependent upon those surrounding it creating a very interactive working environment. Since the bridge is the backbone of the tracker, other team members dictate many of the needed bridge functions and their contributions are appropriately noted.

1.2. OBJECTIVE

This thesis presents the methods used to design a large, welded structure whose primary requirement is a specified minimum resonant frequency. To understand the design choices made, such as the overall geometry of the bridge which greatly impacts the frequency response, details of the many functions that the bridge serves are presented. While these constraints are specific to HETDEX, all structures have a number of design drivers such as volume or mass requirements making each design unique. The principles discussed, however, may be applied to many other designs.

The modeling approach, while not uncommon for such a task, utilizes a number of interesting features to mimic the real world structure. Other designs can utilize these modeling techniques and, as a result, may be of particular interest to the reader. This also applies to the method of constraining degrees of freedom (DOF) in the finite element analysis (FEA) software. Manipulating individual beam form factors to reduce cross-sectional area in one plane in a manner which maintains stiffness in key axes is also demonstrated. For the telescope, this is done to reduce the amount of light reflected off of the bridge prior to reaching the primary mirror, but other applications could benefit from this technique.

1.3. ORGANIZATION

This thesis first reviews prior art for multiple beam theories used to predict frequency response from various types of structural beams. This chapter will also review major lessons learned from the operation of the HET and how those lessons impact the

design of the upgraded system. Chapter 3 describes the HET telescope detailing the bridge's functions, constraints and operating parameters. Chapter 4 describes solid modeling techniques used to design the bridge and its key features. Details of the finite element analyses (frequency response, deflection and stress) are discussed in Chapter 5. Chapter 6 discusses pertinent fabrication processes including welding and the precision machining operations required. Chapter 7 discusses the conclusions of the bridge design and presents areas for future work.

2. Prior Art

Several areas of research were conducted in preparation for this design. A literature review of various beam theories was performed to understand the assumptions and limitations of each theory. The theory utilized by the chosen solid modeling software was studied in detail in addition to the dynamic behavior of thin-walled structural tubing.

Very specific to this design, a collection of lessons-learned is presented regarding MDO's ten years of operational experience with the HET tracker. Areas discussed are limited to those affecting the design of the new tracker. For several areas, topics are discussed in additional detail when describing the bridge in Chapter 3.

2.1. LITERATURE REVIEW

Thin-walled beams are in widespread use spanning many engineering applications. High strength to low weight for a given distance makes thin-walled beams a very attractive solution. The key limitation to these beams, however, is the typically low torsional resistance provided to the structure. Additional bracing, e.g. a supporting truss structure, can improve upon this limitation.

While literature references many beam theories varying in the assumptions and applications applied, there are four widely used theories relating to mathematical models of beams: Euler-Bernoulli, Rayleigh, shear and Timoshenko. According to Han, et. al.

[10], the Euler-Bernoulli theory (18th century), also called the classical beam theory and the engineering beam theory, accounts for two major factors: strain energy due to bending and kinetic energy due to lateral displacement. While this theory is relatively simple to implement, it tends to overestimate the frequency response and is not as accurate for non-slender beams [10]. The Rayleigh theory (1877) [11] improves the Euler-Benoulli theory by accounting for effects of rotation of the beam's cross-section. The shear model adds shear distortion to the Euler-Bernoulli model improving predicted frequency response results [10]. Timoshenko's theory (1921) [12, 13] combines the previous two theories to the Euler-Bernoulli theory incorporating both shear deformation and rotational inertia effects. Han includes a thorough literature survey on these theories and their subsequent use in evaluating various beam models.

A fifth beam theory, the Vlasov theory [14], applies solely to thin-walled beams. Ahmad [15] presents the general assumptions of the theory and the governing differential equations. The elementary beam theories and Vlasov theory share six generalized displacement components: three displacement components, two slopes and the angle of twist. Vlasov theory has a seventh generalized displacement component, the rate of change of the angle of twist with respect to the beam axis [15].

Due to widespread use of thin-walled beams, existing literature covers many aspects of its behavior. Many papers focus on the vibration behavior response of individual beams under various loading and restraining conditions. For example, Banerjee [16] derives exact analytical expressions for natural frequencies and mode shapes of a cantilevered beam coupled in bending and torsion. Prokić [17] derives

governing equations of motion for triply coupled vibrations on thin-walled beams under various end constraints. Prokić and Lukić [18] explore dynamic behavior of thin-walled beams when braced with additional beams in several configurations.

More recently, finite element analysis has become a very popular tool for analyzing beam structures. With many FEA packages available, structural designs can be quickly analyzed to determine the optimal solution. Bakker [19] outlines basic guiding principles and identifies common mistakes when performing FEA on thin-walled members. These principles apply for all software packages and serve as a top level introduction to the many pitfalls which can lead to inaccurate results. An accompanying paper written by Sarawit and co-authored by Bakker [20] discusses the applications of thin-walled member FEA. Topics discussed are types of available analyses, the importance of material property selection, meshing options and initial conditions in addition to providing several examples.

While FEA packages provide a simplified means of quickly analyzing complex structures, each is built upon an algorithm performing the necessary calculations. For Simulation, SolidWorks' built-in FEA program used in this design (previously called CosmosWorks), the beam theory used in development of the software is Euler-Bernoulli (Dassault Systèmes SolidWorks Corp. Technical Support, personal communication, March 9, 2010). Furthermore, the Simulation development team specifically referenced the section concerning beam elements from Przemieniecki [21].

Euler-Bernoulli theory derives the stiffness properties (i.e. the force-displacement relationships) for a uniform beam element from the differential equations for beam

displacements [21]. Assuming the bending planes align with the principal axes, six groups of loads result which can all be treated individually. Figure 2.1 shows the types of loads that can be applied to a beam: axial forces (S_1 and S_7), twisting moments (S_4 and S_{10}), shearing forces (S_2 and S_8), bending moments (S_6 and S_{12}) and another set of shearing forces (S_3 and S_9) and bending moments (S_5 and S_{11}) orthogonal to the first two sets. The resulting displacements created by these loads cause vibrations within the beam. The manner in which the beams vibrate as a system are the natural frequencies which are of utmost interest in the bridge design.

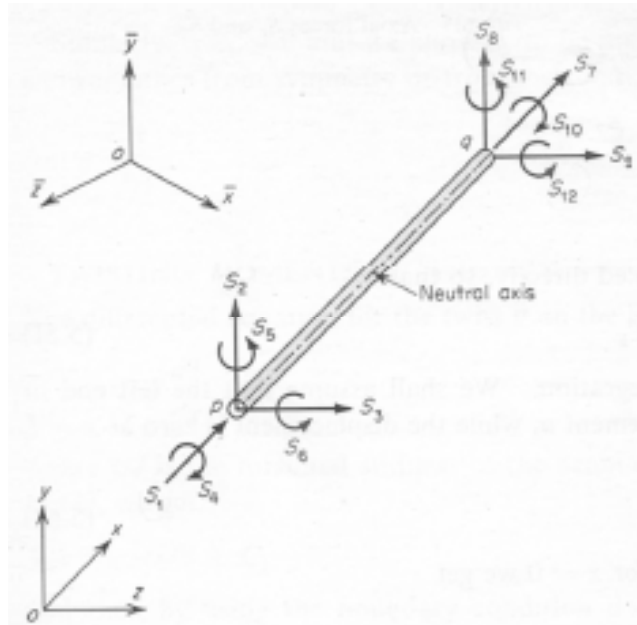


Figure 2.1: Beam element diagram displaying the six groups of loads on a beam

Source: [21, pg. 71]

2.2. HET LESSONS LEARNED

The HETDEX upgrade benefits from the 10+ years of operational experience accrued on HET. It has also been helpful that several original HET design engineers,

namely John Good and John Booth, continue employment at MDO and were available to provide insights and recommendations for improvements. This level of collaboration will lead to a better final design. The following section is derived from numerous meetings with MDO staff throughout the project.

In addition, the creation of a sister telescope in Sutherland, South Africa named the Southern African Large Telescope (SALT) [22-24] has also contributed to the design of HETDEX. SALT, completed in 2005, is referred to as the second generation of HET due to the improvements made based on recommendations from MDO staff. While communications with SALT engineers has been limited, several of their improvements are incorporated into the HETDEX design and are noted in the discussion to follow.

Component stiffness is a key design driver for more than just the bridge. Every component supporting the science instruments plays a critical role in the success of capturing a stable spectrograph image. Experience with the HET design reveals multiple areas on the tracker where stiffness is extremely important, particularly for the hexapod. The hexapod consists of the lower hexapod frame, six electromechanical actuators and the strongback (i.e. the upper hexapod frame). The actuators essentially act as three springs in series: the lower end mount, actuator and upper end mount [25]. The design of each component plays a critical role in the overall function of the hexapod.

The penalty of designing extremely stiff structures is mass. The HETDEX corrector optics are substantially heavier than the HET counterparts, by a factor of approximately 7.5. This in turn requires even greater support structures for mounting and positioning this hardware. For example, to obtain the desired hexapod stiffness of >400

$N/\mu m$, the base plate, end mounts and actuators evolved into substantial components in size with a mass over twenty-one times that of the similar components on HET [25]. Likewise, minimizing deflections in the lower hexapod frame is critical. Unlike the HET design which allows the mounting surface (termed the carriage) to extend several feet below the top of the bridge, the HETDEX frame must remain above the main beams of the bridge. This design requires much greater wall thicknesses to prevent excessive deflections and results in a design with a greater mass by a factor of four [26].

Another requirement developed from operational experience of HET also causes the hexapod actuators to grow in both length and mass. Before beginning science operations each night, the telescope operator calibrates the individual mirror segments of the primary mirror to form as perfect a spherical surface as possible, an operation called "stacking". The mirror segments are also vertically aligned on a less frequent basis, termed "pistoning". Pistoning requires aligning a sensor mounted on the corrector optics to each mirror segment. Due to the amount of tip and tilt allowed by the HET hexapod, the entire perimeter of mirror segments cannot be calibrated with the corrector optics. Technicians must align these segments using hand tools, which is both time consuming and less accurate.

The HET staff desires that the sensors on the corrector optics align all mirror segments. With the addition of two more sensors, the tracker can align all but eight mirror segments. This change requires additional linear travel in the two primary axes and greater angular travel within the hexapod. The greater angular travel results in actuators with longer travel once again increasing the mass of each actuator [25].

Since installation, overall mass of the HET tracker continues to increase. Additional instruments, sensors and electronics have been installed on the tracker along with necessary cables and supporting structures. Due to the difficulty in mounting new hardware on the bridge at altitude, HET staff rarely removes equipment at the conclusion of experiments. The resulting “mass creep” over the past 10 years results in an unknown current weight of the tracker. A similar experience will likely repeat itself during the life of HETDEX requiring adequate overhead in component analysis.

A final critical lesson learned from operational experience is the importance of cooling all heat emitting hardware. Due to the manner in which the telescope operates, stray heat signatures can cause distortion in the spectrograph image. For example, a collection of power electronics mounted to the tracker carriage on HET did not have active cooling. Given the severity of the impact to the image optical quality, the staff implemented an add-on cooling system. The result is an air cooled system requiring flexible duct work of substantial size. The ducting hangs from the tracker and is routed to the dome wall creating substantial light obscuration.

This issue led to a HETDEX requirement that all heat generating equipment must maintain a surface temperature, measured at the device insulation surface, within 0.1 degree of ambient temperature [27]. For any device producing more than 10 W of heat to the atmosphere, provisions for cooling jackets and active cooling using a chilled glycol/water mixture is required. These requirements result in additional hose-runs along the bridge and contribute additional mass, both for the tubing and the larger cable carriers required for the routing.

3. Hobby-Eberly Telescope

Figure 3.1 displays the major components of the HET. The telescope resides in an 86 foot diameter dome with the capability of rotating 360 degrees [3]. The main structure of the telescope, constructed of steel pipes, has a constant zenith angle of 35 degrees [3]. Welded on top of the main structure is the upper hexagon, or "upper hex" for short, which provides the base for the moving components, collectively termed the tracker. Also attached to the main structure via a complex truss structure consisting of 383 nodes and 1747 struts are the 91 hexagonally shaped spherical mirror segments forming the primary mirror, described in detail by Krabbendam et al [4]. Each mirror segment has three DOF allowing the telescope operator to align each of the mirror segments independently to form a uniform spherical shape with a 26.165 meter radius of curvature [3]. This alignment occurs at least once a night aided by the center of curvature alignment sensor (CCAS) located in a 90 foot tower outside of the dome.

The backbone of the tracker is the bridge. The term “payload” references all components mounted on top of the bridge that have the ability to translate the length of the bridge’s main beams. The science payload is a subset of the overall payload and consists of the corrector optics necessary to capture and focus the light which reflects off of the primary mirror. Following is a description of the bridge functions and key

telescope components mounted to the bridge. Both the current and new HETDEX bridge constraints are presented as well as key parameters that dictate how the bridge operates.

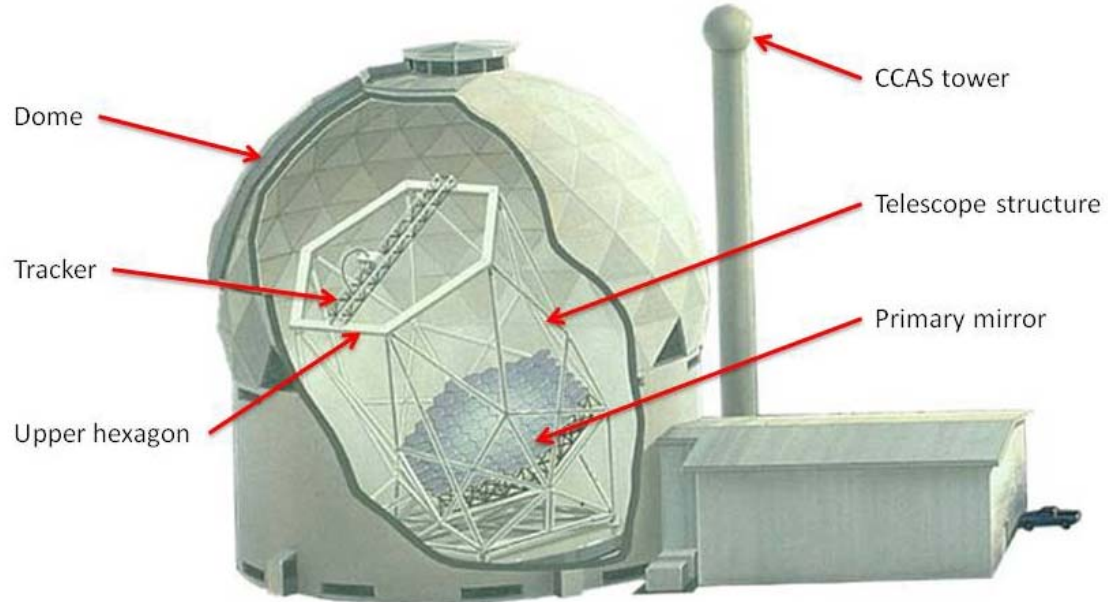


Figure 3.1: Cutaway rendering of the Hobby-Eberly Telescope revealing the primary components

Source: [1] (labels added)

3.1. BRIDGE FUNCTIONS

The tracker translates along two legs of the upper hex via a drive system consisting of a pair of planetary roller screws and linear bearings shown in Figure 3.2. A second pair of linear bearings mounts on top of the two main bridge beams. This allows the payload to translate via a third roller screw. The tracker coordinate system referenced throughout this thesis is also shown in Figure 3.2. The tracker translates along the X-axis on the upper hex while the payload translates in the Y-axis along the length of the bridge. The Z-axis is normal to the upper hex and main bridge beams, which is 35 degrees from the gravity vector. The telecentric optical axis, W-axis, is the corrector optics' optical

axis which tips and tilts to remain on a spherical focal surface matching the surface of the primary mirror. When the tracker is centered over the primary mirror, the Z and W axes are coincident. Manipulating the corrector optics requires three rotational DOF. These DOF are theta (rotation about the X-axis, or tip), phi (rotation about the Y-axis, or tilt), and rho (rotation about the W-axis) [28].

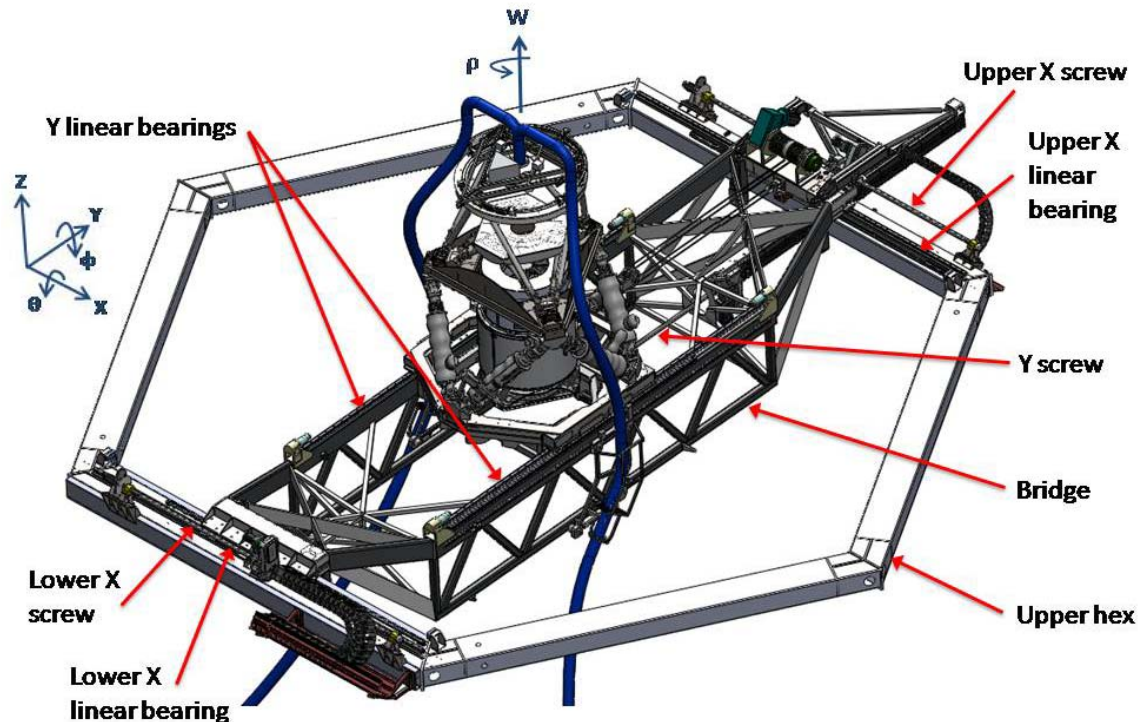


Figure 3.2: SolidWorks' screenshot of upper hex with full tracker and coordinate system displayed

Source: CAD model created by HETDEX team

The bridge supports the payload mass and consists of several key components, illustrated in Figure 3.3. Not shown in this figure are the many additional instruments, sensors, shrouds, cables and hoses that exist as part of the final payload. While the analyses account for the masses and locations of these components, the illustration shows

a simplified view to provide clarity. The following describes these components as originally conceptualized by engineers at MDO.

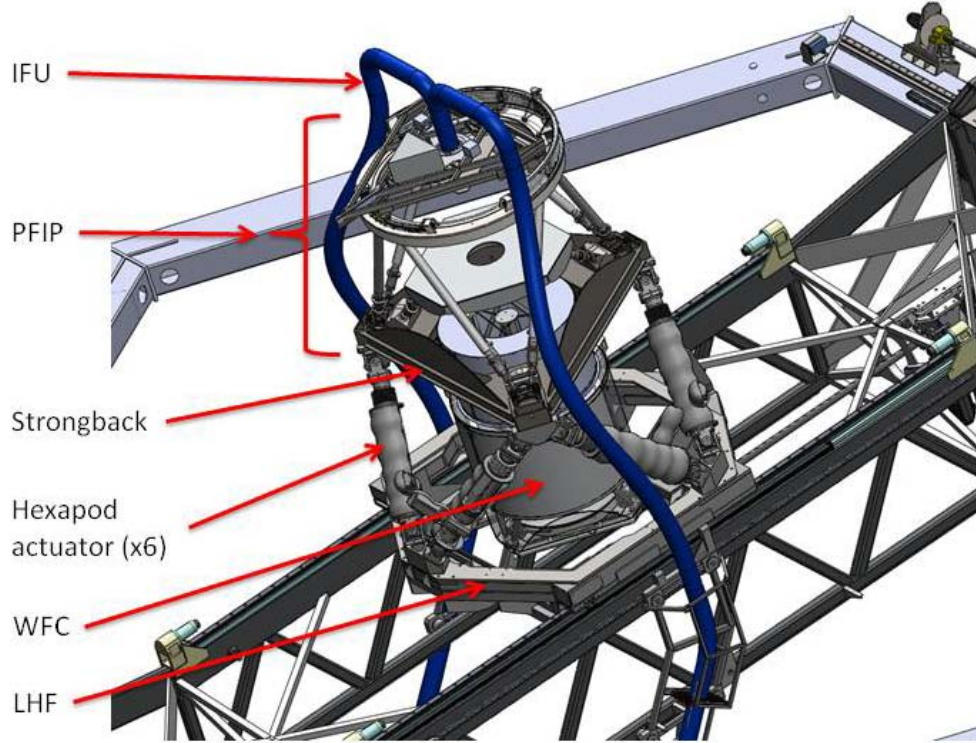


Figure 3.3: Screenshot of the simplified HETDEX payload and hexapod actuator arrangement

Source: CAD model created by HETDEX team

The wide field corrector (WFC) is the first optical instrument which acts to focus light reflected from the primary mirror [29]. The entrance pupil of the WFC must be positioned exactly at the primary mirror's prime focus and aligned to the mirror's principal axis. As the telescope tracks a star, the tracker slowly moves in either the X, Y or both axes. Since the surface of the primary mirror is spherical, the entrance pupil must follow a spherical path, called the focal surface. This is accomplished via a hexapod providing six degrees of freedom to the WFC and the subsequent corrector optics mounted above, collectively named the prime focus instrument package (PFIP).

The hexapod actuators mount to the lower hexapod frame (LHF) and the strongback, which also supports the WFC. The PFIP mounts above the strongback, whose optical components act to further focus the light collected by the primary mirror. The light finally enters a collection of 96 integral field units (IFU) which house fiber optic cables [30]. Light passes through the fiber optic cables and is then analyzed in one of 96 visible IFU replicable unit spectrographs (VIRUS), specifically designed for HETDEX [30-32].

IFUs are a major addition to the original HET design. The current HET utilizes three spectrographs: the Low Resolution Spectrograph, which is mounted on the tracker, and the Medium and High Resolution Spectrographs located in the basement of the telescope [30, 33]. Two bundles of fiber optic cables hang from the tracker down to the Medium and High Resolution Spectrographs. For HETDEX, locating 96 spectrographs close enough to the tracker to prevent light degradation within the fiber optic cables poses a significant challenge, in addition to simply routing the IFUs to each spectrograph. The impact of using so many spectrographs with respect to the bridge is threefold: 1) the bridge must support additional hardware to route the IFUs towards their respective spectrograph cabinets, called the fiber management system (FMS) [34]; 2) the sum total of the fiber optic cables and their sheathing causes a significant loading not present on the original tracker; 3) the IFU bundles cause concern of additional loading during high wind conditions which may excite a natural frequency of the telescope.

The portion of the FMS that interfaces with the bridge is the pair of carriages that mount to the sides of the bridge, Figure 3.4. The carriages consist of stress relieving

hardware to prevent additional strain on the IFUs' connection point at the top of the PFIP and acts as a guide to minimize swinging loads as the payload translates. Each carriage rides on a pair of linear bearings allowing the carriage to translate with the payload. One bearing rail mounts to the outside of the bridge's main beams and the other mounts underneath the lower beam of the bridge. This arrangement is identical on both sides of the bridge.

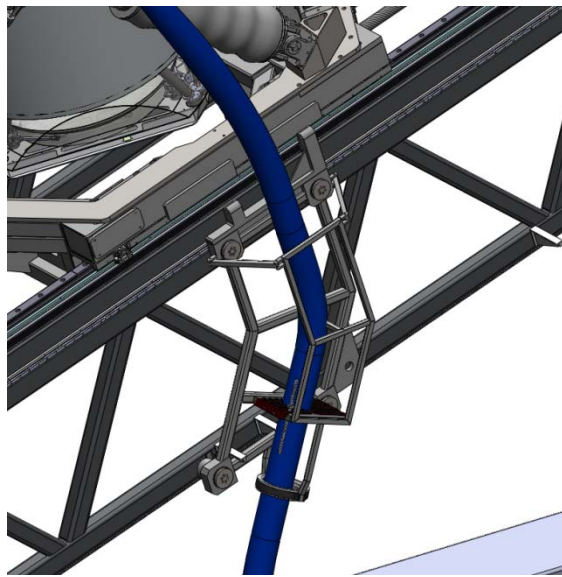


Figure 3.4: FMS carriage mounted to the side of the bridge guiding an IFU bundle

Source: CAD model created by HETDEX team

Supporting the Y-axis roller screw is another key function of the bridge, Figure 3.5. The screw's nut rigidly attaches to the payload and both ends of the screw mount to the bridge via the screw's bearing housings. In this manner, whenever the nut or screw is driven, the payload translates along the bearing rails.

A final requirement of the bridge is to interface with multiple cable carriers. Given the vast array of electric motors, instruments and sensors mounted to the bridge, a

large number of cables and hoses must be routed from the upper hex onto the translating bridge. A cable carrier attaches to both the upper (UX) and lower (LX) sections of the upper hex which extend and retract along the X-axis. The cables and hoses then run along the bridge to the specific devices. All cables and hoses terminating on the moving payload pass through the LX carrier. These cables feed along the bridge and then enter the Y-carrier (visible immediately to the left of the roller screw in Figure 3.5). The free end of the Y-carrier attaches to the payload.

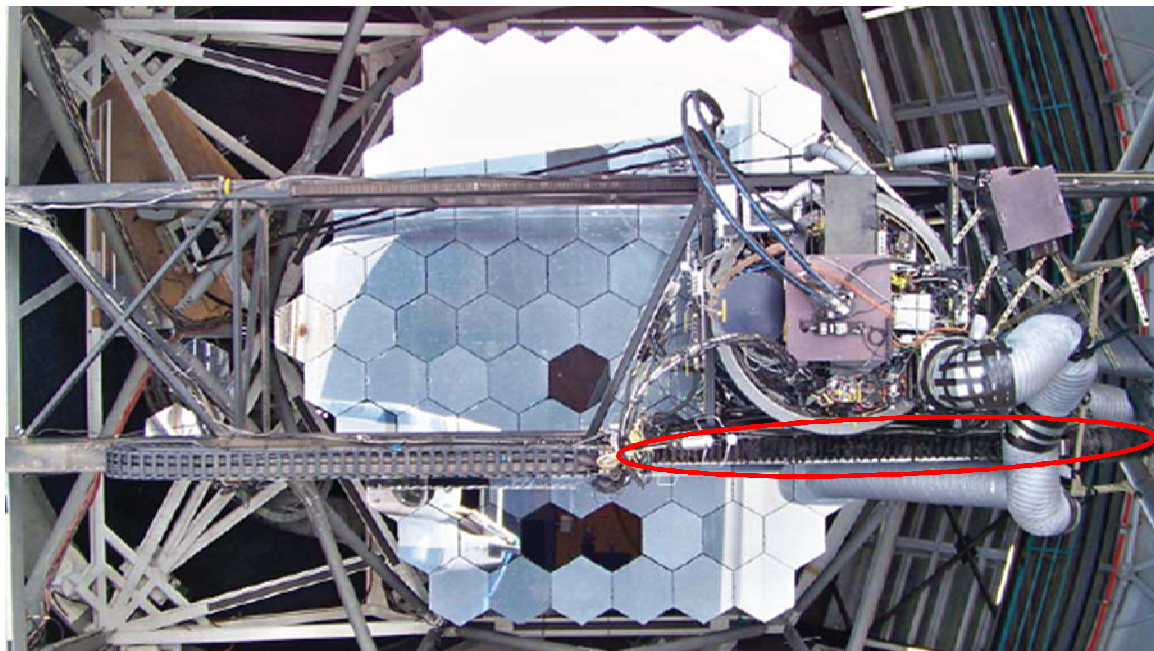


Figure 3.5: Overhead view of the HET Y-axis roller screw mounted above the primary beam of the bridge

Source: McDonald Observatory [2]

Throughout the design process of the bridge, each of the above functions impacts the design in varying degrees. The more critical functions will be discussed in additional detail in the following sections.

3.2. EXISTING CONSTRAINTS

A number of constraints remain constant from the HET design. For a ground up design these would be variables, but there are no plans to significantly modify the upper hex or supporting framework. The most obvious of these constraints is that the HETDEX bridge will maintain the same 35 degree mounting angle. This angle has a significant effect in how the weight of the bridge distributes to the upper hex.

Maintaining the upper hex's dimensions also fixes the distance between the X-axis linear bearing rails. The distance between the LX and UX bearing rails is 10,647 mm [35], establishing the minimum length requirement for the bridge. While the bridge could overhang the bearing rails, it definitely cannot be shorter.

In addition, the length of the upper hex sides remain fixed at a distance of 6143 mm [35]. This constraint limits the bridge width due to the required corrector optics rotational range of ± 8.5 degrees in theta and phi for science operations, which equates to a linear travel of 1770 mm [36]. Additional travel is built into the system for margin, after which stopping distances are added. The total travel allowed for the HET bridge is approximately 3900 mm [36]. Due to the nearly symmetrical primary mirror, the travel requirements are identical in both the X and Y axes. In addition to the travel limiting the bridge width, it also generates a requirement for the length of linear bearing rail needed along the bridge's main beams (Y-axis).

The primary mirror's radius of curvature establishes the key Z-axis dimension. The WFC entrance pupil must be accurately located at the mirror's prime focus, a distance equal to half of the radius of curvature (13.08 meters) [3]. Since the distance

between the vertex of the mirror and the top of the upper hex is fixed, the upper hex provides a convenient reference point for the bridge design. Many additional variables contribute to locating the top of the main bridge beams with respect to the top of the upper hex. As previously mentioned, the strongback supports the WFC which in turn is positioned by the hexapod. A parallel design effort of the LHF, hexapod and strongback by other CEM engineers (Ian Soukup and Joseph Zierer) eventually established the height of the main bridge beams.

The primary mirror of an optical telescope captures light emitted from stars much like a bucket collects rain. Unlike a rain bucket, the light reflects off of the mirror to a central point, the WFC entrance pupil. Obstructions mounted above the primary mirror casts shadows upon the mirror, effectively blocking that amount of light from ever reaching the mirror. Obscuration is the measure of light being blocked, and is usually expressed as a percentage of total mirror area. The push for designing telescopes with ever larger primary mirrors allows astronomers to study stars further from Earth.

A certain amount of obscuration is unavoidable since the tracker must be mounted directly above the primary mirror to position the corrector optics. The corrector optics' geometry alone forms a circular "hole" in the primary mirror referred to as central obscuration. The size of central obscuration changes depending on the tracker's position relative to the primary mirror and ranges between a 2 to 2.5 meter diameter circle on the current HET. Central obscuration increases to an approximately four meter diameter circle due to the wider viewing angle of the HETDEX optics [37]. The effective aperture

of the primary mirror with the HETDEX optics is 10 meters as compared to HET’s 9.2 meters somewhat offsetting the greater central obscuration [37].

Additional obscuration outside of this circle totaled 3.2% of the primary mirror area during HET’s original construction [28]. Over the life of the telescope, obscuration increased with the need to add additional sensors, instrumentation, and cooling systems. Minimizing obscuration received scrutiny throughout the HETDEX tracker development despite not being provided a specific goal. This requirement affected not only the design of the bridge, but also the placement of every piece of hardware onto the bridge (e.g. the Y-axis cable carrier, roller screw, etc.).

3.3. HETDEX CONSTRAINTS

HET personnel identified areas of improvement for incorporation into the HETDEX upgrade [38]. Some of these changes involve improving maintenance accessibility while others stem in response to various failure modes encountered over ten years of operation. Numerous changes directly impact the bridge design.

Hexapod mounting arrangement became one of the most impactful requirements established by the MDO staff with respect to the new bridge. The HET hexapod and supporting framework is nestled within the width of the bridge [28], as illustrated in Figure 3.6. This design creates a compact volume envelope for the payload, which in turn reduces overturning moments when the hexapod positions the payload in full tilt conditions (approximately 8.5 degrees from vertical). The bridge and hexapod design

drove the location of the upper hex (in terms of the Z-axis) allowing the main bridge beams to remain straight beams across the entire span.

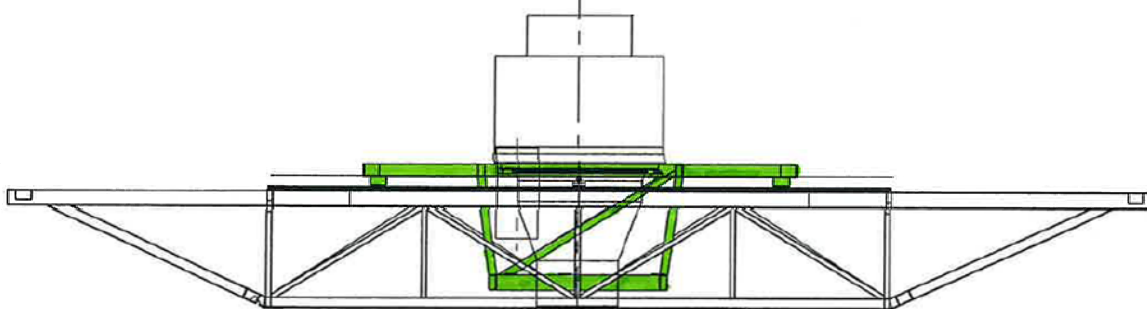


Figure 3.6: The nested hexapod actuators (not shown) attach to the upper and lower members of the carriage (highlighted in green) on the HET tracker

Source [39]

Relocating the hexapod above the bridge became a key requirement for HETDEX to greatly improve maintenance access [27]. The truss section of the new bridge drops below the top of the upper hex to maintain the same location of the WFC pupil. As a result, the HETDEX bridge more closely resembles the SALT bridge in overall geometry as shown in Figure 3.7. The center of gravity (CG) of the new, taller and heavier payload raises substantially above the bridge's main beams due to the new design. The Y-axis linear bearing rails are sized to counteract the tilting moment as the hexapod swings the science payload through its spherical range of travel.

The new hexapod design has one other critical impact to the bridge design. The upper and lower mounts of all six actuators lie on a circle. To provide the most optimal load transfer from the actuators to the LHF and ultimately to the bridge, four actuator mounts align directly above the main beams. This couples the width of the bridge directly to the diameter of the hexapod mounting circle.

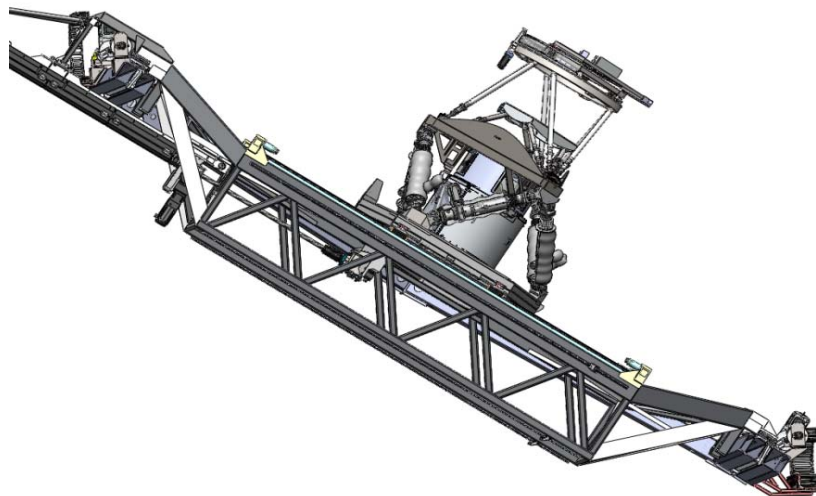


Figure 3.7: Photo of SALT tracker (top) & SolidWorks' screenshot of HETDEX tracker showing how the main bridge beams angle downwards from the upper hex

Sources: SALT photo by John Good, McDonald Observatory; CAD model created by HETDEX team

Travel requirements for HETDEX (identical for both the X and Y axes) dictate the main bridge beams' length. This in turn specifies the angle needed to join the main trusses to the end sections of the bridge above the upper hex. As travel increases, the incline becomes steeper having a definitive impact on the bridge's frequency response.

HETDEX travel requirements increase compared to the original HET design. After experiencing multiple failures, the HET staff desired to implement another set of mechanical limit switches near the end of travel in the X and Y axes. The first set of limit switches trigger the software system to begin braking by reducing current to the drive motor(s). The new limit switches trip a software independent power interrupt to the motors and engages pneumatically actuated disc brakes on the roller screws. While this addition eliminates software related failures occurring in the past, it requires additional braking distance on all bearing rails. The placement of hard stops allows the system to come to a full stop after triggering either limit switches. Table 3.1 shows a comparison of the travel requirements.

Table 3.1: Travel comparison between HET and HETDEX

Parameter	Units	HET		HETDEX	
		X & Y	X	Y	
Science range*	mm	± 1770	± 1768	± 1768	
Limit switch #1	mm	± 1880	± 1850	± 1850	
Limit switch #2	mm	N/A	± 1880	± 1880	
Hard stop	mm	± 1970	± 2020	± 2000	

* Science range is the travel equating to a ± 8.5 degree science payload tip and tilt

Sources: HET [36]; HETDEX [27]

Another major difference between tracker designs is the mounting arrangement of the Y-axis roller screw. The HET Y-screw mounts above the primary rail of the bridge, previously illustrated in Figure 3.5. The primary beam is made from an $8 \times 6 \times \frac{3}{8}$ in. hollow structural section (HSS) tube while the secondary beam is a $6 \times 6 \times \frac{1}{4}$ in. HSS tube [40]. The bearing arrangement on the carriage allows the primary rail to be the guide rail

and the secondary rail simply provides a rotational restraint [28]. The screw's drive nut rigidly attaches to the carriage, which is the payload's main support structure. The primary beam is sturdier as it also carries the moment induced from the offset mounted drive [28]. Typically, linear bearing manufacturers prefer that the distance between the drive screw and one bearing rail is no less than one third the distance between the rails [41]. A pair of bearing blocks support the carriage on the primary rail while only a single block exists on the secondary rail which has an additional DOF in the X-axis [28].

Originally, the intent for the HETDEX bridge was to mimic the HET Y-screw location. At SALT, the Y-screw mounts on the outside of the bridge's primary rail as shown in Figure 3.8. Despite these two examples of working systems, the HETDEX design evolved into an entirely different concept.

Figure 3.9 shows the center pull Y-drive for HETDEX, led by CEM design engineer Nick Mollison [42]. The primary motivation for utilizing this approach stems from relocating the hexapod above the bridge beams. Joseph Zierer performed a detailed design study to determine the optimal mounting arrangement of the six electromechanical actuators for the hexapod [43, 44]. The most favorable actuator loading configuration pairs the actuators' mounting points as shown in Figure 3.3. Unfortunately, this causes an interference with the volume previously occupied by the Y-drive directly above the primary beam. Mounting the screw either inside or outside of the bridge, like the SALT design, was considered but the obscuration impact became too significant.

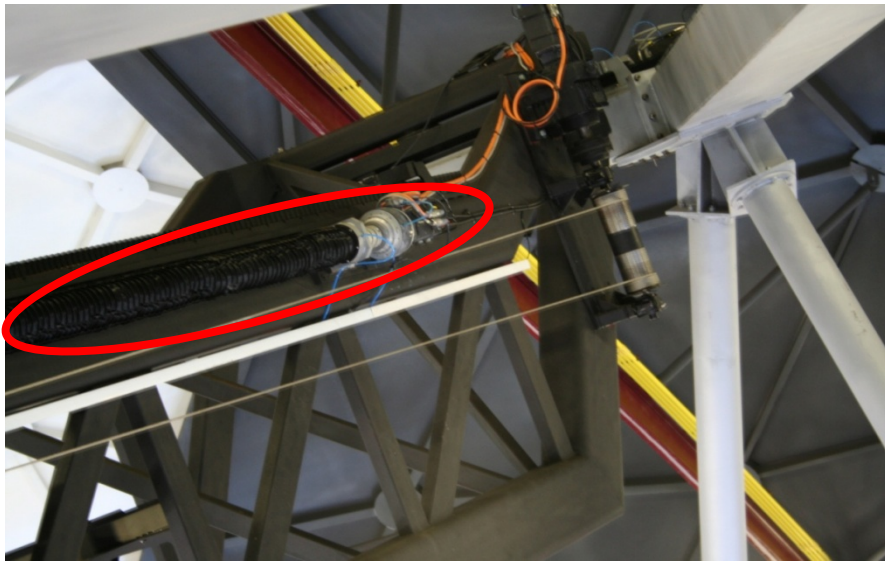


Figure 3.8: SALT bridge showing the location of the Y-screw outboard of the primary beam

Source: Photo by John Good, McDonald Observatory

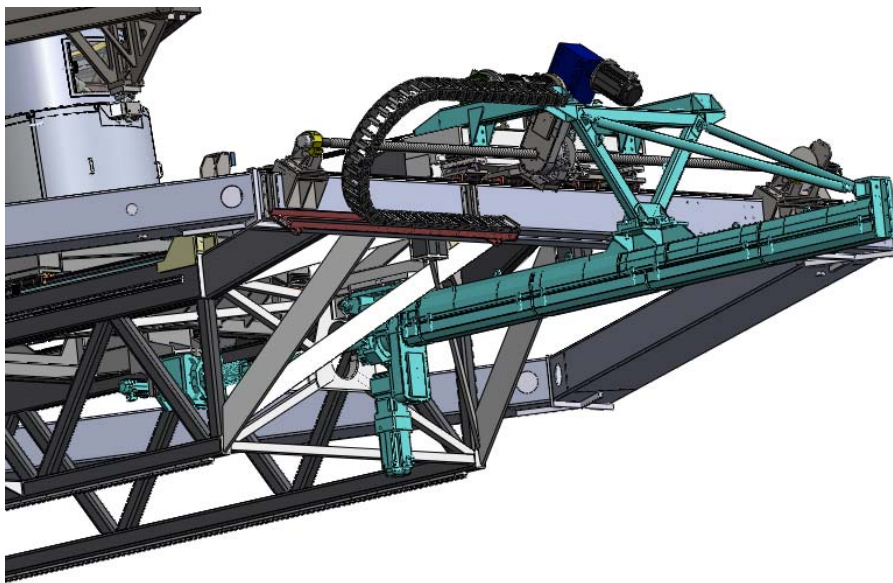


Figure 3.9: HETDEX center pull Y-drive assembly (highlighted in light blue)

Source: CAD model created by HETDEX team

Mounting the screw on the centerline of the payload also provides a more favorable loading condition on the linear bearing blocks. The HET payload is supported by three bearing blocks, two on the primary rail and one on the secondary rail. Due to the

significantly greater payload mass, the center pull design allows for the mass to be distributed between four bearing blocks. The linear bearings are also larger, 65 mm rails versus 45 mm on HET, increasing the load carrying capacity to account for the heavier payload [45].

The center pull drive needs a means to support the free end of the screw. A structure extends out from the upper end of the bridge and ties onto the end of the screw housing. With this arrangement, the nut remains stationary on the underside of the bridge and the screw translates with the payload through its travel. One end of the screw mounts to the LHF via a spherical bearing while the other end mounts to a linear bearing block, allowing the floating end to translate with the payload [42].

A key improvement over the HET design utilized at SALT is the inclusion of a constant force drive (CFD) [46]. The CFD consists of a wire rope cable running along the outside of the bridge beneath the Y-axis roller screw, visible in Figure 3.8. One end of the cable attaches to the carriage and translates with the payload. The other end wraps around a spool at the upper end of the bridge, controlled by a constant torque drive. As the carriage translates either up or down, the CFD drive responds to sensors on the cable and spools out or reels in cable accordingly. The cable system supports 80 percent of the payload's weight offloading the Y-axis screw [47].

While reducing the load driven by the Y-axis screw is the primary goal of SALT's design to allow the use of a smaller drive motor, an added safety benefit exists as well. At HET, one major failure occurred which led to the carriage free falling down the length of the bridge. Given the large amount of money invested in the corrector optics carried

by the carriage, this scenario is one of the telescope’s worst case failures. The HETDEX CFD operates foremost as a safety device and as a performance device second [42]. Both the roller screw and CFD have the capability to support the entire payload independently. In this manner both systems have to fail simultaneously for another free fall event to occur. The bridge design provides features to incorporate the CFD system.

3.4. OPERATION PARAMETERS

The telescope’s normal operation modes are not factors in terms of the structural design of the bridge. The tracker has two distinct modes: tracking and slewing. When conducting science operations, the tracker focuses on a celestial object and translates only to counter the earth’s rotation while tracking that object. Per the HETDEX Critical Dimensions and Masses document [45], maximum tracking velocity is 3 mm/s, although for most operations it is substantially slower. This speed applies to movement of the bridge, payload and/or hexapod actuators. During maintenance procedures and gross adjustments in tracker position, a maximum slewing velocity of 80 mm/s is possible. The controlled acceleration and deceleration rates are 20 mm/s^2 and 0.5 mm/s^2 for slewing and tracking respectively [45].

Due to the nature of the redesigned corrector optics as part of the HETDEX upgrade, initial estimates increased the science payload mass by a factor of four. The original HET science payload² measured approximately 440 kg [28], although that mass

² HET science payload consists of the optical package, spherical aberration corrector and the prime focus instrument package

increased over the years of operation due to the addition of numerous instruments and experimental hardware. The HETDEX estimated science payload³ is 3160 kg, which is an increase of over seven fold from HET [48]. Supporting hardware for the heavier payload, such as the hexapod actuators and mounts, also experienced a significant mass increase to support the heavier payload. Table 3.2 shows a comparison between the original HET design goals⁴ and the HETDEX hardware as of this writing (line items are paired with their respective counterparts between the designs). The bridge's increased payload CG height became a major design driver for the bridge.

The heavier payload impacts the bridge design in two distinct ways, both of which are chief concerns: natural frequency and deflection. To successfully analyze light from a star, the corrector optics must be held stable. Vibrations in the tracker induced from either the drive systems or wind gusts can cause pixel smear rendering the data useless. Stray heat signatures from electrical equipment or even heat released from objects within the telescope dome as ambient temperature decreases during the night can cause enough thermal distortion to affect the image.

Experience with HET reveals that the drive systems are not a common trouble source while tracking due to the very slow speeds. Effects from the wind, however, can have a significant impact due to the unpredictable and random occurrence of gusts. In

³ HETDEX science payload consists of focal surface assembly, rho-stage, pupil assembly, WFC and its instruments, electronics, focal plane and pupil assembly supports, and thermal control system

⁴ Masses of the actual hardware used on HET could not be obtained from MDO

addition to establishing conditions when the telescope must shut down, designing a very stiff tracker is the best defense to avoid wind related imaging issues.

Table 3.2: Comparison of HETDEX and HET component masses

HETDEX Component	Mass [kg]	HET Component	Mass [kg]
IFU Mass Loading On PFIP	260	Rotary Stage	70
Focal Surface Assembly	584		
Rho-Stage	403		
Pupil Assembly	116	Optical Package	150
Wide Field Corrector	873	Spherical Aberration Corrector	90
WFC Instruments	80		
Electronics	353	Prime Focus Instrument Package	200
Focal Plane Assembly Support	279		
Pupil Assembly Support	378		
Hexapod System	2079	Hexapod System (base, actuators, platform)	139
Strongback	850		
Lower Hexapod Frame	2300	Carriage	573
Y-Drive System	913	Y-Drive	80
Constant Force Drive	597		
Bridge	7577	Y Beam (bridge)	2154
FMS Loading on Bridge	610		
Y Cable Carrier	141	Y Cable Carrier	91
Thermal Control System	90	Misc.	91
Work Platforms	400		
TOTAL TRACKER BRIDGE	18,882	TOTAL TRACKER BRIDGE	3638

Sources: HETDEX components [48]; HET components [36]

The HET design team established 10 Hz as the minimum first mode natural frequency for the bridge [36]. Subsequent experience proves the tracker is sufficiently stable at this design value. Analysis calculates the entire telescope support structure with the HET tracker has a resonant frequency of approximately 4.5 Hz [47]. Safe telescope

operation requires the bridge's first mode natural frequency be significantly greater than the overall telescope's first mode. The design value of 10 Hz was again provided as the requirement for the HETDEX bridge [27]. This is a substantial requirement given the large increase in mass of the payload.

The other key performance requirement of the bridge that the payload mass directly impacts is the deflection of the bridge beams as the payload traverses the length of the bridge. Since the WFC entrance pupil must always remain on the focal surface, the hexapod must compensate for deflections in the bridge. Limited travel in the hexapod actuators require a bridge deflection limit of 2 mm [27, 36]. Calculating this value requires subtracting the bridge's self-weight deflection with no payload from the worst case Z-axis deflection in the bridge beams under full payload.

4. Solid Modeling

The bridge design uses typical CEM design processes and tools. The solid modeling portion of the design utilizes SolidWorks, a popular 3D mechanical computer aided design (CAD) software package [49]. The structural and frequency analyses are performed using SolidWorks built-in FEA platform, Simulation (formally called CosmosWorks).

The design process is inherently iterative. The SolidWorks/Simulation package provides a key advantage in that it utilizes a single model for both the design effort and for analysis. As the Simulation analyses identify improvements, or as the design adapts to other components changing within the system, the solid model is updated and then quickly reanalyzed. Other 3D CAD packages require two distinct models, one for the solid model and another for analysis. This requires the designer to replicate any changes independently in both software packages, effectively slowing the design process. Some packages allow the solid model to be exported from the CAD platform and imported into the FEA model, but this conversion can lead to a loss of fidelity and/or features in the overall model.

4.1. BRIDGE DESIGN

To meet the requirements and functions discussed in Chapter 3, the bridge needs to maximize stiffness, minimize mass, be relatively easy to fabricate and be cost effective. Given the success of both the HET and SALT bridges, the team gave little consideration to a different construction method. The plan was to utilize a welded truss-like structure constructed of thin-walled HSS tubing and evolved over time as the design of mating components matured and as requirements changed.

The bridge is modeled within the SolidWorks' environment utilizing the weldment tool in lieu of traditional modeling techniques such as boss extrusions and cuts. The framework, or skeleton, of the bridge is drawn using a series of 2D and 3D line sketches. Creating sketch profiles of various rectangular and square tubing sizes within the weldment profiles library allows for quick insertion into the model. These profiles are extruded down the length of the sketch lines. During subsequent FEA runs, the skeleton and/or the sketch profiles are easily modified if additional or less stiffness is required in specific planes.

While creating the skeleton, it quickly became obvious that an assumption must be made regarding the subsequent analyses. While sketching the skeleton, all of the endpoints of the sketch lines are coincident. Common endpoints become joints between the beam members upon meshing the model in Simulation. This style of node-to-node modeling, while very straightforward, lacks the reality of how the beams will be welded and results in two issues. First, when beam profiles are extruded the length of the sketch lines, overlapping of material occurs at the joints. SolidWorks' weldment tool provides

methods to trim excess material but Simulation prevents the use of these tools to successfully mesh the model. For the bridge, this results in approximately 250-300 kg of excess mass being analyzed. The second issue is that fabrication limitations sometimes require that beams be welded in locations which do not provide the desired node-to-node joints. In many of these instances the beams were later positioned in the actual fabrication locations and the analysis was rerun. The net effect on the frequency results of six of these fabrication modifications was a decrease in the first mode frequency of 0.3 Hz.

Prior to the first critical design review (CDR) held on December 16-17, 2008, the bridge design specified all thin-walled HSS tubing. While the design was close to the natural frequency requirement, overall obscuration was deemed too great. While details of cable carriers, screw placement, etc. had not been finalized and their resulting obscuration directly accounted for, the fear of beginning with so much obscuration concerned MDO engineers.

John Good, an MDO engineer and CEM's primary engineering contact on this project, analyzed the current status of the bridge and made a series of recommendations to modify the existing tubing. Locations of beams were unchanged but beam form factors were manipulated while holding cross sectional properties nearly constant. For example, the ends of the main trusses of the bridge are joined by a group of beams termed the bulkheads, Figure 4.1. These bulkheads were originally constructed of 8x6x $\frac{1}{4}$ in. horizontal tubing and 6x6x $\frac{1}{4}$ in. diagonal tubes but were changed to 2 $\frac{1}{2}$ in. solid square bars. Likewise the "X-bracing" near the ends of the bridge were 6x6x $\frac{1}{4}$ in. tubes and are

now 1x9 in. plates. The results are nearly equivalent beams in terms of stiffness in the key planes but have substantially smaller cross-sectional areas in the X-Y plane.

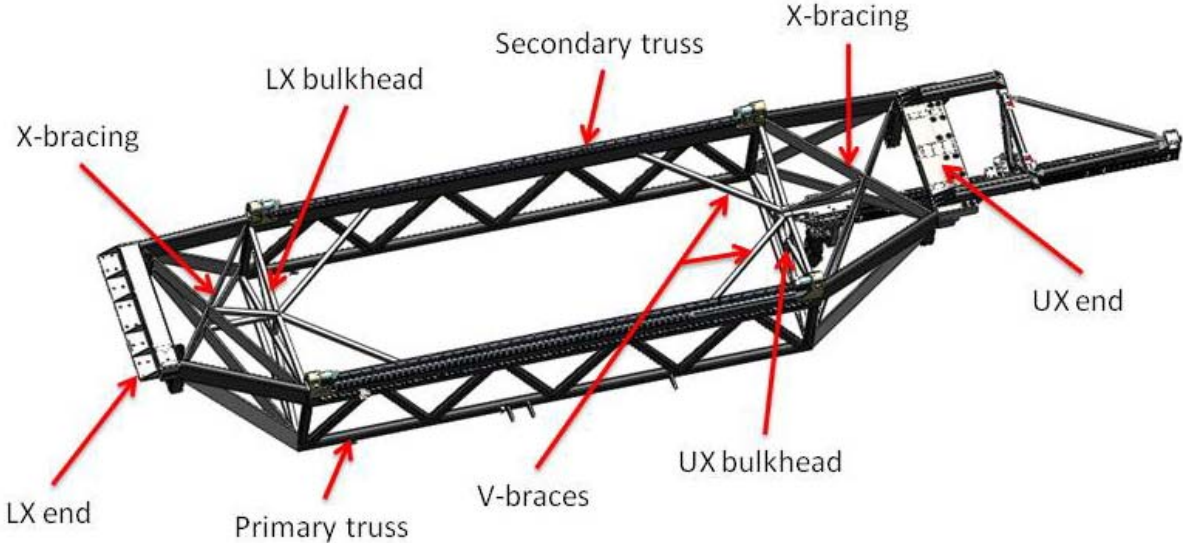


Figure 4.1: Current bridge with labels of main sections

Viewing the bridges from above readily reveals the overall effect of Good's recommendations, Figure 4.2. The first image shows the original design and the second image is after Good's modifications. Calculations reveal on-axis obscuration decreases from 12.1% to 5.1% [50]. The changes require making a mass compromise of almost 25 percent in exchange for the obscuration reduction. An additional modification suggested by Good modifies the payload modeling approach to better reflect existing DOF while also increasing realism to the bridge loading. All parties received these changes well and became incorporated into the design.

Placement of beams remained essentially unchanged but beam form factors continued to be modified for better frequency response as the design matured. This was particularly helpful due to increases in payload mass experienced as other components'

designs developed. Due to the position of the payload, these mass gains cause an adverse effect on the bridge's frequency response. The relocation of the Y-drive also required changes to the bridge.

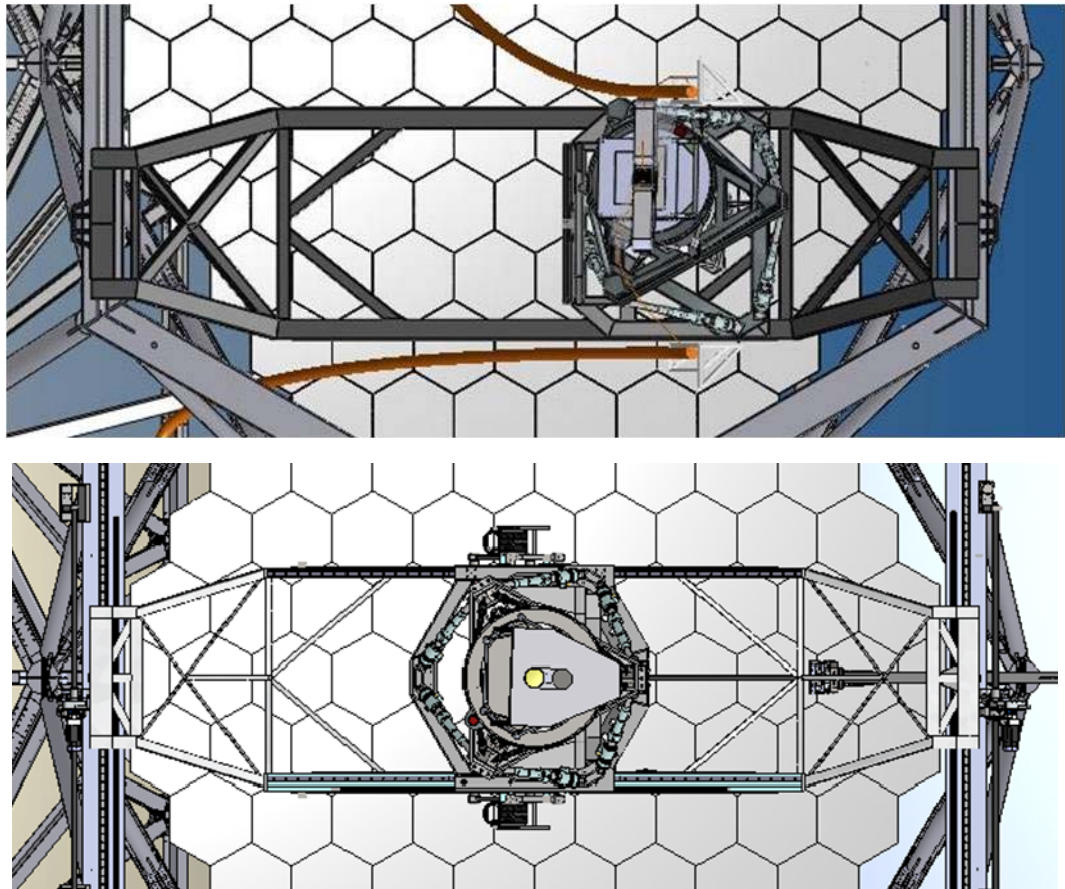


Figure 4.2: Bridge design constructed completely from HSS members (top) and redesign optimizing obscuration utilizing bar, plate and HSS members (bottom)

Source: CAD model created by HETDEX team

4.2. KEY FEATURES AND GEOMETRY

This section outlines the details of various beams used to create the bridge. The most intricate areas of the bridge are the upper and lower end sections which interface the X-axis linear bearing rails. This geometry depends on the respective bearing arrangements

and will be described in detail in Appendix B, which discusses the FEA model constraints.

4.2.1. Main Bridge Sections

The bridge's main beams are each constructed with a pair of rectangular box tubes, Figure 4.3. The primary beam consists of two $12 \times 4 \times \frac{5}{16}$ in. tubes welded together lengthwise while the secondary beam is fabricated from two $12 \times 2 \times \frac{1}{4}$ in. tubes. Due to the load supported by the linear bearing rails, the main bridge beams are doubled so as to provide a stiffening member beneath the rails. A single 12×8 in. beam on the primary side would require substantially thicker walls to prevent deflection across the width of the beam.

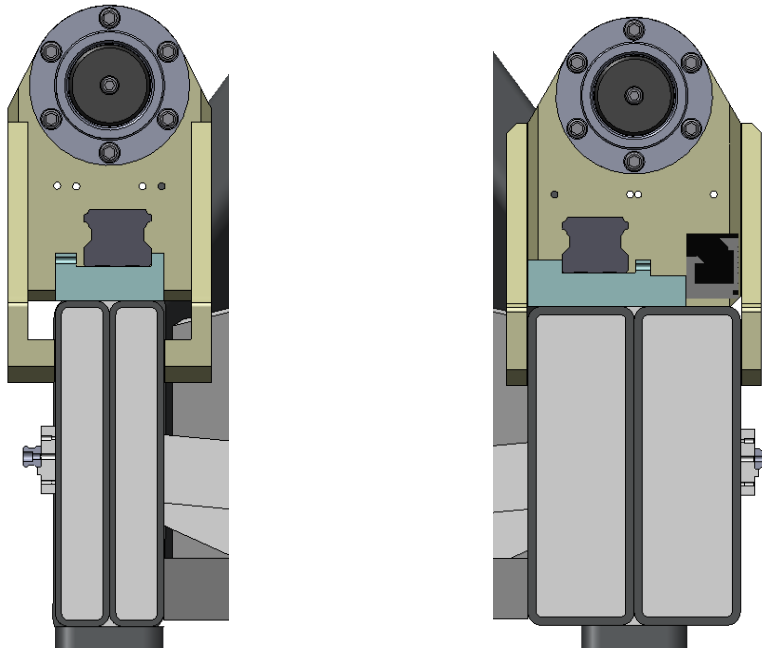


Figure 4.3: Section views of the secondary beam, left, and the primary beam, right. Evident are the main linear bearing rails and ways (light blue), the FMS linear bearing rails and ways welded to the sides of the beams and the bumpstop mounts in the background.

Source: CAD model created by HETDEX team

Similar to the HET bridge, it was felt that having one beam structurally dominate the other would still provide a benefit even with the center pull Y-drive. The Y-axis linear bearings on the secondary rail have an additional DOF in the X-direction decoupling the secondary rail from reaction forces. As a result, the primary beam bearing blocks reacts these forces to the rail.

Steel bars welded along the top of both main beams provide material for machining the linear bearing way details. The box tubing walls are too thin to directly bolt the rails thereby requiring this additional material. The THK SHS65 linear bearing rails fasten to the bridge with M16x2 socket head cap screws [51]. The bar stock welded to the bridge is therefore 32.5 mm thick after final machining to provide sufficient tapped-hole depth for the fasteners. Bar stock on the primary beam also has mounting features to support the linear encoder used to track the payload's position along the Y-axis. For similar reasons, additional stock material is welded and later machined to the outer side of the main beams to mount the smaller FMS linear bearings (THK SHS20 bearings).

The lower beams of both main truss sections are constructed of $5 \times 4 \times \frac{3}{8}$ in. box tubes. Additional bar stock is welded and machined to the bottom of these beams to mount the other FMS linear bearing rails (THK SHS25). The angled truss beams and the vertical beams at the ends of the trusses are $4 \times 4 \times \frac{3}{8}$ in. tubes. Early in the bridge design, three different common truss configurations were analyzed: vertical supports, Warren truss and a Pratt truss [52]. The Warren truss produced a slightly improved frequency response with a lower mass and was therefore ultimately chosen. Throughout the design

iterations, the distance between the upper and lower truss beams was a variable. The primary penalty for adding height to these main trusses is extra mass.

As previously mentioned⁵, the truss bulkheads are constructed from 2½ in. solid square bar stock. The bulkheads form an “X” with additional supporting members above and below. The lower bar is straight but the upper bar is cut into two separate pieces. These bars slope downwards towards the center of the bridge to create clearance for the LHF. While this complicates modeling and fabrication, the frequency response impact was essentially negligible.

Prior to the rearrangement of the Y-drive, the upper and lower bulkheads were identical in construction. Both have a few additional members of bar stock to increase stiffness. A vertical member is used to join the center of the “X” to the upper bars and two bars tie the bulkhead to the “X-braces”. The members which dramatically increase stiffness are the “V-braces”. These members are not desirable from an obscuration perspective, and created an interference with the LHF which was later resolved. The increase in stiffness provided by these members, however, is significant enough to accept the consequences.

Adapting to the new center pull Y-drive configuration required several modifications. To locate the end of the screw and to more accurately model the effect of the payload’s high CG, a mock LHF is introduced to the model. The LHF is modeled as an “H” frame using 2x2x^{3/64} in. tubes, as seen in Figure 4.2. Thin tubes are used so that

⁵ Section 4.1, pg. 35

the mass, totaling 15 kg, does not have to be subtracted from the payload, which includes the mass of the real LHF. Attached to the center of the frame is a large, hollow cylinder whose mass and CG characteristics match the payload. Extending from the upper beam of the LHF is a triangular group of $2 \times 2 \times \frac{3}{64}$ in. tubes representing the track drive housing which is welded onto the LHF. This allows the screw to be mounted in the correct location with respect to the bridge.

The payload consists of many individual components as is readily evident by the mass table of major subsystems previously shown in Table 3.2⁶. These various components were designed and incorporated into the solid model by multiple engineers from both CEM and MDO. The bridge was to be analyzed with the payload at the position causing the lowest frequency response, i.e. the worst case scenario. Originally, the payload was positioned at the midpoint of the main beam span. In later analyses, the payload was shifted so that its CG was directly above the midpoint of the main beams representing the worst case scenario regarding frequency response. This requires shifting the LHF 900 mm upwards along the main beams to account for the mounting angle of 35 degrees.

The roller screw is modeled as a solid 60 mm diameter bar, matching the actual screw diameter. After analyzing several configurations proposed by Mollison, the team determined that mounting the Y-drive underneath the bridge provides the best location for installation/removal and maintenance access.

⁶ Section 3.4, pg. 31

This decision required modifying the upper bulkhead so that the screw could pass through the bulkhead. The center of the “X” is cut out and $\frac{3}{8}$ in. reinforcement plates are used to tie the four diagonal bars together, Figure 4.4. In addition, one of the horizontal bars tying the bulkhead to the “X-braces” is replaced with a much larger plate for mounting the Y-drive. This bracket also serves as the rigid connection point for the slew drive assembly and screw nut. Subsequent analysis performed by Mollison ensured there would not be a sacrifice of stiffness in this area.

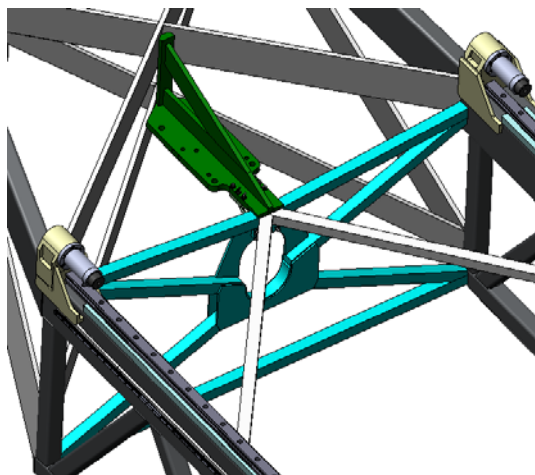


Figure 4.4: Upper bulkhead (blue) and mounting bracket (green) for the Y-drive, slew drive assembly and roller screw nut

Source: CAD model created by HETDEX team

Different parameters establish the width of the main trusses and the width of the end sections above the X-axis linear bearings. The hexapod mounting circle drives the main truss spacing whereas the travel requirements on the upper hex limit the available width for the bridge ends. These two widths differ by 848 mm. As a result, not only do the members tying the main trusses to the bridge ends have to angle upwards, but each also has to angle inwards resulting in a compound angle.

The upper members in these sections are $12 \times 4 \times \frac{3}{8}$ in. box tubes and the lower members are 1x9 in. plates. The upper and lower corners of the main trusses are tied to the end sections with the “X-braces”, also constructed from 1x9 in. plates. In all of these areas, the smaller material dimension is oriented to minimize obscuration.

4.2.2. End Sections

The ends of the bridge have seen the most iterations throughout the bridge design. The LX end is shown in Figure 4.5 in its final configuration with the upper plate semi-transparent. Formerly constructed entirely of rectangular box tubing, this subassembly is now fabricated with $\frac{1}{4}$, $\frac{3}{8}$, $\frac{1}{2}$, 1 and $1\frac{1}{4}$ in. thick plates welded together.

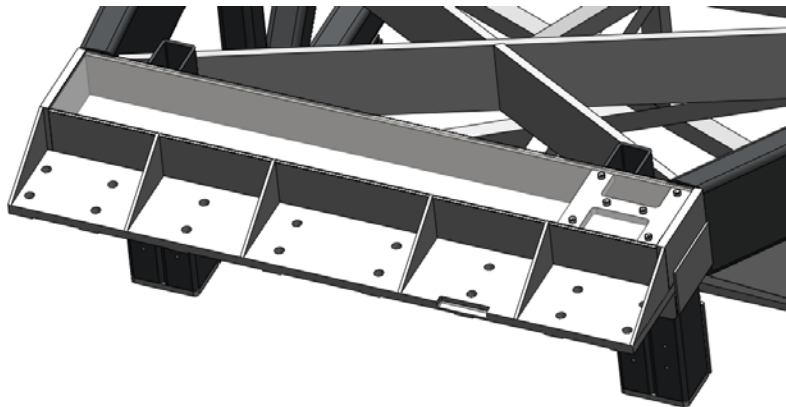


Figure 4.5: LX bridge end with top plate shown semi-transparent to reveal the 'H' shaped LX cable handler bracket attachment point

During integration onto the upper hex, a major interference was encountered with the LX screw and slew drive housing, Figure 4.6. When operating in slewing mode, a DC permanent magnet motor turns the nut through a belt and pulley system while the screw is held stationary by a pneumatically operated disc brake. During tracking, a separate motor mounted to the end of the screw rotates the screw while the nut is kept

from rotating via a separate brake. This dual drive system allows each motor to be custom sized for a narrow operating range. Tim Beets, a CEM design engineer, developed the slew drive and then began the process of integrating it into the system.

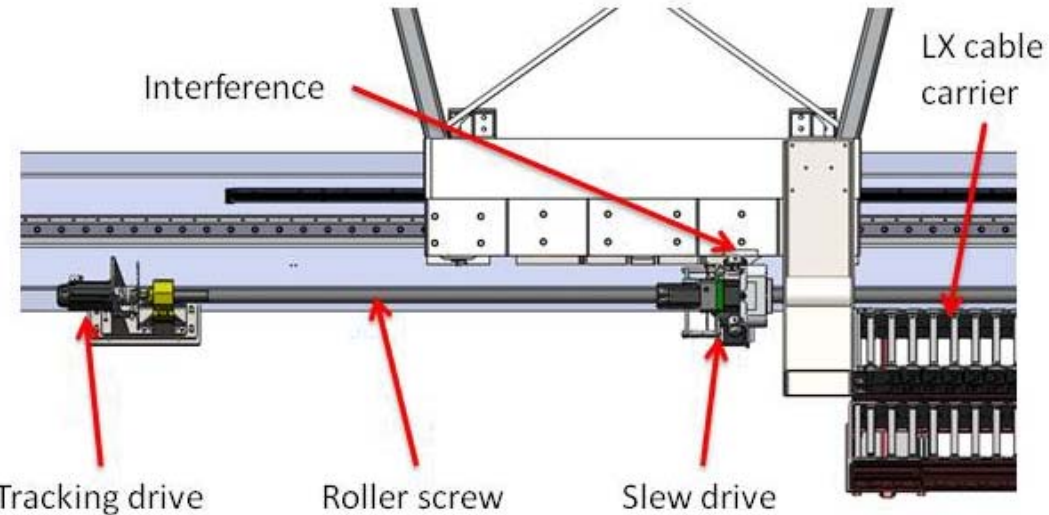


Figure 4.6: Top view of the LX bridge end showing the roller screw, slew drive and tracking drive
Source: CAD model created by HETDEX team

The CEM design team desired to mount the roller screws as close to the linear bearings as possible to eliminate the need of reacting large moments from the nut to the linear bearing blocks. Due to the size of the slew drive, the options were to extend the screw further away from the linear bearing rail or to modify the end of the bridge. The latter was chosen after a configuration was found which did not sacrifice stiffness across this very important section of the bridge. A large cutout down the length of the bridge end eliminates the majority of the interference. The lowest plate of the end section was increased to $1\frac{1}{4}$ in. thick plate to maintain stiffness and $\frac{3}{8}$ in. thick ribs were added. The hole pattern in the lower plate is for M24x3 bolts which fasten the bridge to the bearing

block mount plate. The mount plate in turn is attached to the linear bearing blocks providing the bridge its necessary DOF.

The LX bridge end must adapt to the X-axis cable carrier. One end of the cable carrier is fixed to the upper hex. Cables and hoses are routed up the telescope support structure and enter the cable tray at this location. The other end of the tray connects to and translates with the bridge. A bolt hole pattern is drilled into the LX bridge end to attach the cable tray. Additional material is needed for the tapped bolt holes so a thicker piece of steel is welded to the inside of the bridge end as shown in Figure 4.5.

The UX end section serves the same function but with a few differences: 1) the slew drive does not cause interferences; 2) due to the taller bearing stack-up the bottom plate of the bridge is raised upwards; 3) additional mounting features are required due to the support structure for the Y-drive and CFD. The UX end section can be seen with the upper plates semi-transparent in Figure 4.7.

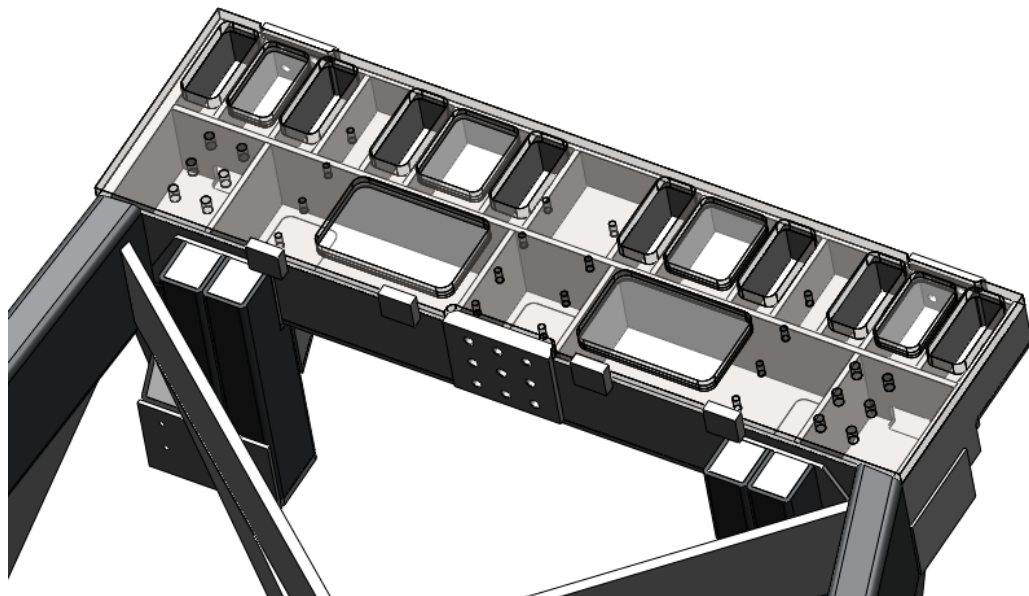


Figure 4.7: UX end section with the top plates shown semi-transparent to reveal internal bracing

The UX end section is constructed of $\frac{1}{4}$, $\frac{3}{8}$, $\frac{1}{2}$, 1 and $1\frac{3}{4}$ in. welded plates. The main base plate is split since one section of the bridge end is raised 80 mm to accommodate the bearing stack. As with the LX end, the bridge is attached to the bearing mount plate via 16 M24x3 bolts. Due to the height of material above the mount plate, cut-outs are made through the upper plate to provide access to the bolt holes in the lower plate preventing the need for long fasteners. Internal ribs are welded into the structure next to these cutouts to maintain stiffness. Unlike the LX end, the upper plate was made thick enough to be directly drilled and tapped. The Y-drive support beams are bolted to the outer ends and the CFD skid is bolted across the top. Additional cutouts are made in the upper plate simply to reduce weight and are replaced with much thinner plates to maintain stiffness. Pulleys for the stationary end of the CFD wire rope are mounted to the back side of the UX end section and must react the load supported by the CFD.

4.2.3. Y-Drive Support Structure

As previously mentioned⁷, the entire Y-drive system, including the support structure, is designed by Nick Mollison [42]. It is important to discuss the details of this support structure as one of the primary natural frequencies changed mode shapes after the addition of the center pull Y-drive.

Extending from the top of the UX end section of the bridge is a pair of 6x6 in. HSS tubes, each constructed of two 6x3x $\frac{1}{4}$ tubes welded together. These weldments

⁷ Section 3.3, pg. 26

bolt onto the bridge creating a modular assembly, allowing for simpler initial installation of the bridge onto the upper hex. The other ends of these bridge supports are joined via a support truss, a triangular group of $4 \times 3 \times \frac{1}{4}$ in. tubes tying the braces to the main Y-drive support, Figure 4.8. In addition, two support struts, NPS 2 in. SCH 80 pipes, extend from the main braces out to the end of the Y-drive housing and attach via spherical rod ends. The Y-drive housing itself is a weldment made from a $2 \times 3 \times \frac{1}{4}$ in. tube with $1\frac{3}{4} \times \frac{1}{2}$ in. bar stock welded along the bottom side and a $2 \times \frac{1}{2}$ in. bar standing vertical welded to the upper side. The lower piece of bar stock serves as the way for a THK SHS30 linear bearing. The roller screw bearing housing is bolted to the linear bearing block allowing the screw to translate with the payload. The sides of the housing have hinged access panels down the entire length for maintenance accessibility. The Y-drive housing ends at the slew drive housing which is bolted to the bridge near the X-bracing.

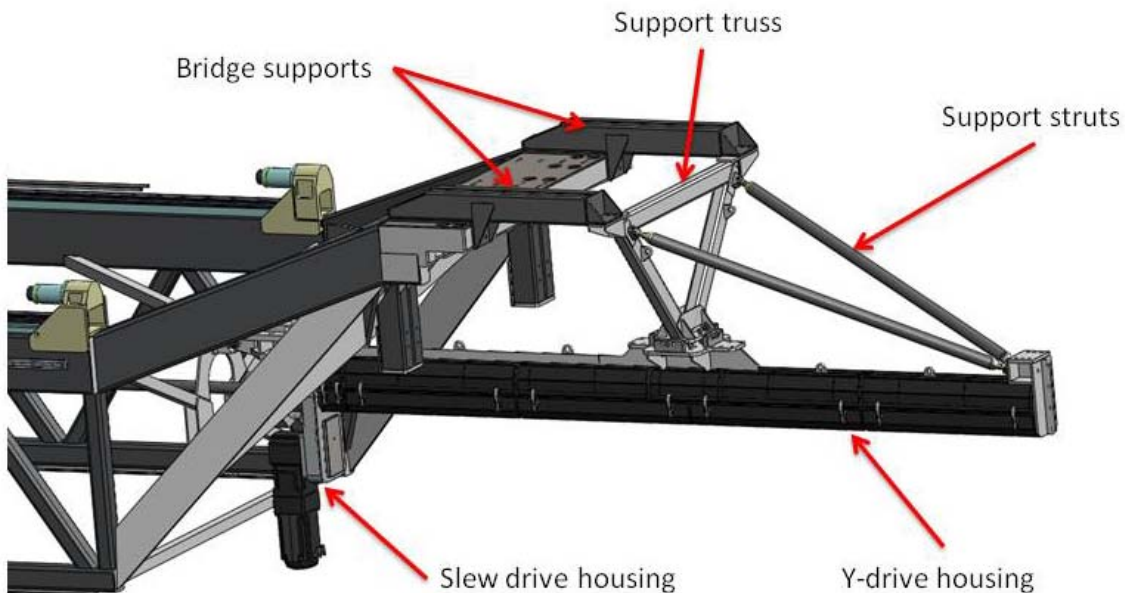


Figure 4.8: Y-drive support structure extending from the UX bridge end

Source: CAD model created by HETDEX team

5. Finite Element Analysis

Determining the type of mesh to use for an FEA is an important decision. The type of analysis, model complexity and desired results all play a role in making that decision. Given that many of the bridge beams are HSS thin-walled tubes, attempting to perform a solid mesh with sufficient mesh density across the wall thicknesses over such a large structure would require considerable computing power and long run times. A beam mesh, however, converts the beam elements into an array of “stick figures” with the appropriate cross-sectional properties. The result is a very quick running analysis ideal for this type of design. Figure 5.1 shows the meshed bridge ready for analysis.

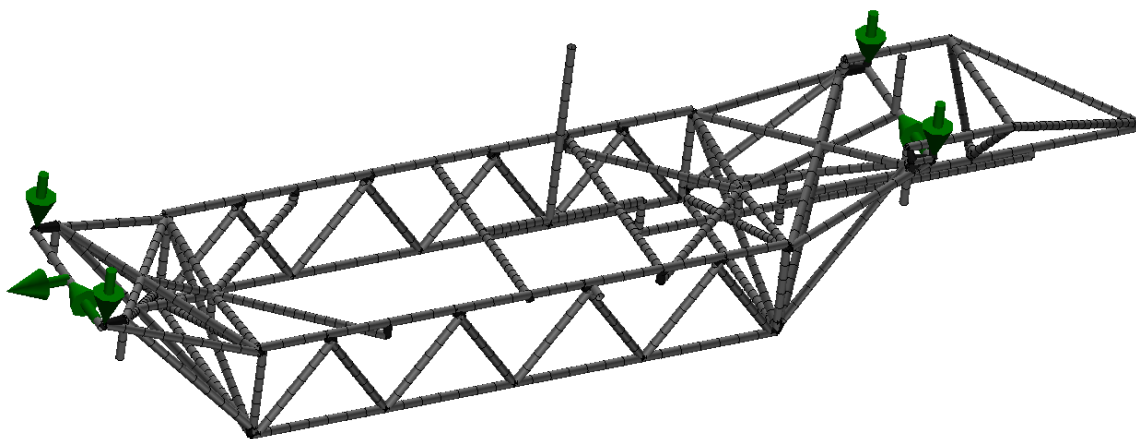


Figure 5.1: SolidWorks’ Simulation mesh of the bridge with applied constraints shown (green arrows)

Utilizing the beam mesh analysis requires modeling all parts of the bridge with beams within SolidWorks. This complicates the modeling effort in areas such as the

bridge ends which will be fabricated from steel plates, not HSS tubing. Custom sketch profiles are created to resemble the cross section of the bridge ends and are extruded across the width of the bridge to create a beam which could then be analyzed in Simulation.

The model requires several manipulations to more accurately reflect the real bridge prior to analysis. The bridge will be in its final assembly state when it is mounted atop the upper hex and potentially excited by wind gusts. This means that in addition to the bridge itself, all subassemblies will be installed on the bridge. The main subassemblies are the payload, Y-drive, CFD and FMS carriages. These subassemblies are treated in various ways within the model as detailed in Appendix A.

Figure 5.2 shows a comparison of the fully modeled tracker bridge and the beam analysis version. Upon close inspection, the simple beam counterparts for the payload, CFD, anti-skew blocks, hard stops, FMS carriages and Y-drive can all be seen.

An FEA model's results are only as accurate as the constraints established. Analyzing the real structure and mimicking the proper constraints within the software's capabilities is one of the more difficult aspects of FEA. The bridge's modeling constraints changed over time due to increasing the level of detail within the model and as features of the bridge changed during the design process.

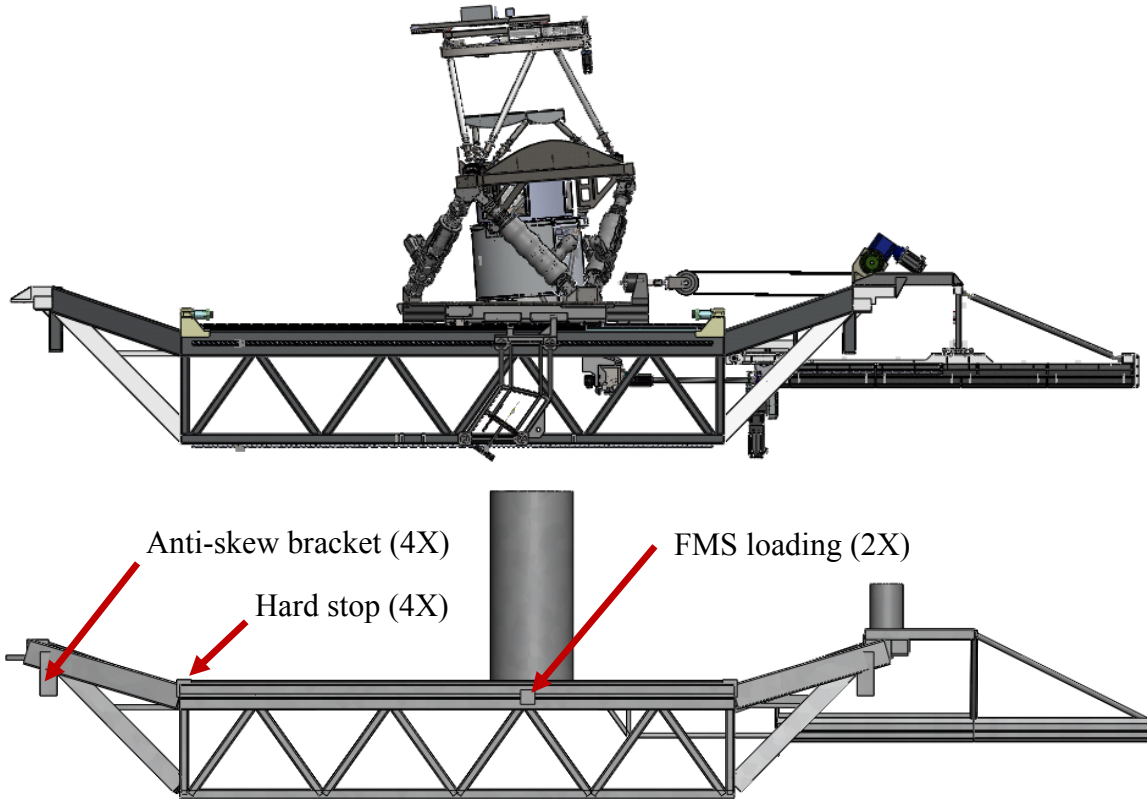


Figure 5.2: Comparison of the tracker bridge model (upper) to the beam model created for FEA

Source: CAD model created by HETDEX team

To understand why the specific constraints are chosen, one must have a fundamental understanding of how the bridge is restrained to the upper hex and the payload. Other features of the bridge are modified as well to more accurately reflect the bridge in the virtual world. Appendix B provides the details needed to prepare the bridge for the natural frequency, deflection and stress analyses.

In summary, the constraints applied within Simulation to replicate the existing DOF are shown as green arrows in Figure 5.1. At the center of the LX end, a constraint is applied which prevents translation in the X and Y axes. This constraint represents the skew bearing. The constraint at the center of the bridge on the UX end only prevents X-

axis translation (assuming the roller screw brakes are applied). Y-axis translation is allowed due to the DOF provided by the short Y-rails. On the corners of both ends of the bridge, additional constraints are applied which prevent translation in the Z-axis, representative of the HCR bearings.

Table 5.1 displays the final results from the finite element analyses performed on the bridge. The details of each analysis and the results are discussed in additional detail in the following sections.

Table 5.1: Summary of FEA results

Parameter		Units	Value
Natural Frequency	1 st	Hz	9.40
	2 nd	Hz	10.72
	3 rd	Hz	13.70
Delta Deflection		mm	1.506
Von Mises Stress		MPa	48
Buckling Load Factor		---	-7.61

5.1. NATURAL FREQUENCY ANALYSIS

Throughout the bridge design process, the natural frequency analysis drove the majority of the iterative changes. The frequency response was the key design driver, making the frequency model the primary design tool. SolidWorks allows the model to be quickly setup for analysis: apply constraints, modify material properties per the changes outlined in Appendix A, create joints between beams and finally mesh the model. At this point, the model is ready to be run and due to using the beam mesh, processing time routinely takes less than one minute.

5.1.1. Design Process

Simulation outputs mode shapes based on the analysis which can be viewed as animations. The first five mode shapes are studied, with the greatest attention paid to the first three. The first mode by definition has the lowest resonant frequency and is considered the most critical. Mode shapes indicate which areas of the bridge require stiffening to either change the mode shape or to raise the natural frequency within that shape.

While the first five mode shapes retain consistent shapes throughout most of the design process, it was not uncommon for the order to rearrange as design changes were made. This reveals which bridge beams are particularly sensitive to changes and may prove beneficial if specific mode shapes are desired.

The major design change that impacts the first five mode shapes most dramatically is the addition of the center pull Y-drive. The sharp increase in mass, most of which is cantilevered from the UX end of the bridge, introduces several new modes to the analysis. The first mode retains its shape even with this change. As additional changes are made to the design, subsequent modes continue to switch order but the overall shapes remain the same.

While the primary goal of the design process is to increase the first mode natural frequency, the design has to be optimized for multiple parameters. Overall mass and obscuration remain key considerations to monitor throughout the process. The linear bearings have load limitations to meet required life expectancy and while additional

stiffness can be achieved with the use of beams with greater cross sectional properties, the obscuration produced would be counter-productive to the telescope's operation.

5.1.2. Final Results

In the middle of the design process, CEM upgraded SolidWorks to the latest software release and the design continued. A significant difference was immediately seen in the frequency response of the bridge. A detailed modeling validation was conducted as described in Appendix C. The results conclude that SolidWorks seems to overestimate the predicted first mode frequency by almost 10 percent. Due to the tight coupling between the solid modeling and analysis efforts, the decision was made to continue using SolidWorks for the analysis keeping this important caveat in mind.

SolidWorks allows the user to scale results to more clearly depict the mode shapes. The mode shapes and magnitudes for the first three modes are shown below with the deformation scale noted. Since the animations reveal so much more information than screen captures, the images below show the bridge at two separate intervals of the animation overlaid on top of one another. The images showing the bridge at the extremes are semi-transparent for clarity. The colors display the magnitude of vibration, with the scale shown for reference.

To also aid understanding of the mode shapes, multiple views of the bridge are shown for the same mode. Overhead and side views are shown with the exception of the third mode which is clearly depicted with only the side view. For reference, the primary

bridge beam is located on the bottom of the overhead views and in the forefront for the side views.

The first mode, Figure 5.3, measures 9.40 Hz. Attempting to describe the mode shape, it is a combination of what is commonly referred to within the team as the “snake” and “heave” modes. The snake mode creates an ‘S’ shape down the length of the bridge, as can be seen from the overhead view. The heave description references a vertical (Z-axis) flexing motion of the main bridge trusses that can be seen in the side view. In this particular mode, the primary bridge beam experiences greater displacement in both the positive and negative Z-directions (8.53 mm [0.34 in.] max deflection compared to 5.95 mm [0.23 in.] for the secondary beam). Raising this frequency will require stiffening the main bridge rails in both the X-axis to reduce the snake mode and the Z-axis to reduce heaving. This can be accomplished by utilizing larger box tubes and/or increasing wall thicknesses. Both of these changes will increase mass and possibly have a negative effect on obscuration. The overall maximum deflection seen in the first mode is at the tip of the payload measuring 11.51 mm [0.45 in.].

From the mode shapes, particularly the overhead view, the beam releases (discussed in Appendix B) applied to the LHF members are very evident. As the main trusses flex, the ends of the LHF beams can be seen translating in both the X and Y axes. This movement is representative of the bearing arrangement on the LHF. The roller screw also has substantial movement along the X-axis, particularly the section extending from the slew drive to the LHF.

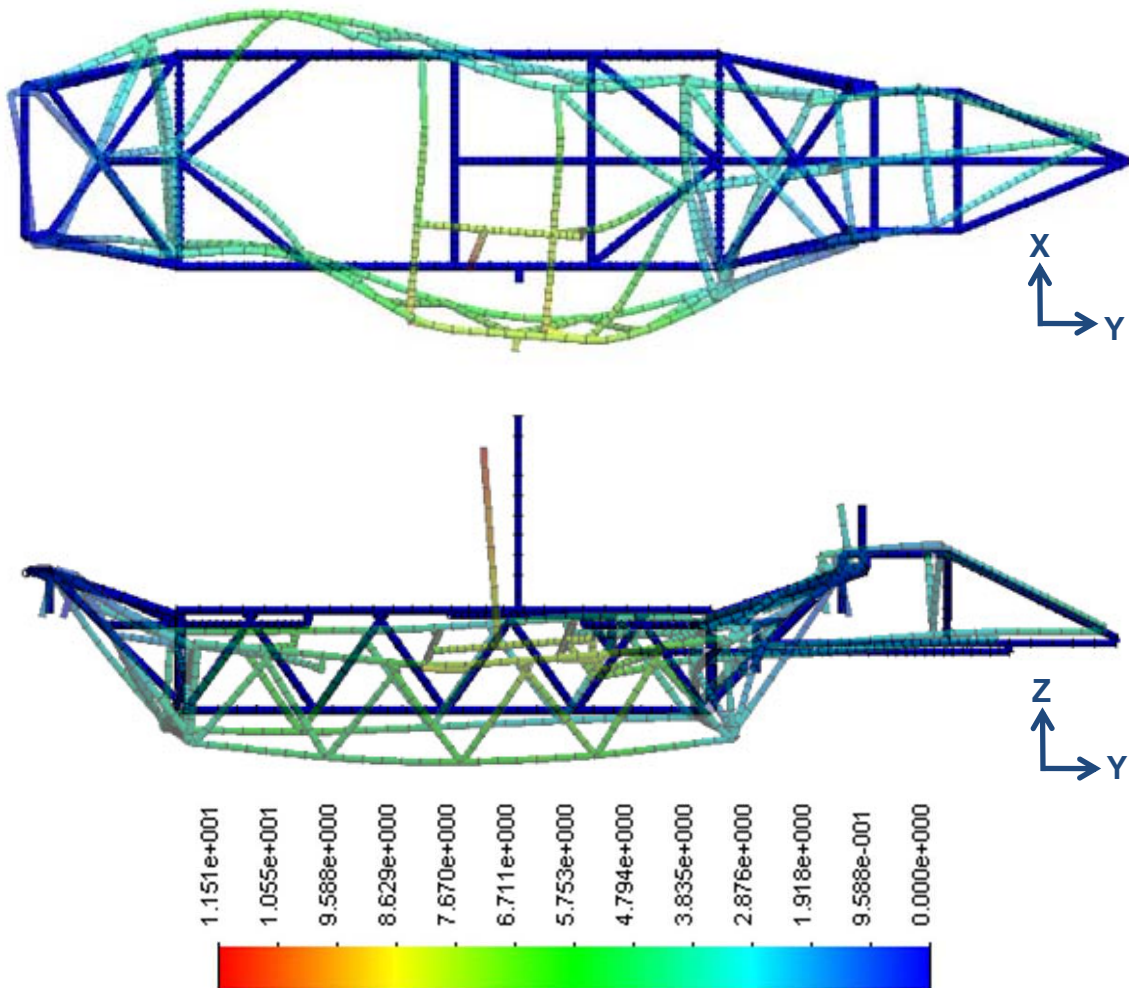


Figure 5.3: Overhead and side views of the first mode frequency response (units = mm, deformation scale = 125)

The second mode, 10.72 Hz, Figure 5.4, behaves very similar to the first mode. The mode shape is again a combination of the snake and heave modes. The main difference is that the secondary bridge beam experiences a greater amount of heave than the primary beam (8.15 mm [0.32 in.] vs. 7.08 mm [0.28 in.] max deflection). Another difference is that in the second mode the Y-drive extending out from the bridge deflects in a similar manner as the UX end of the bridge, meaning the entire structure moves

together. The Y-drive remained almost perfectly within the X-Y plane in the first mode. The approach mentioned to stiffen the first mode should also contribute favorably in stiffening the second mode. The tip of the payload is once again the location of maximum deflection measuring 10.15 mm [0.40 in.].

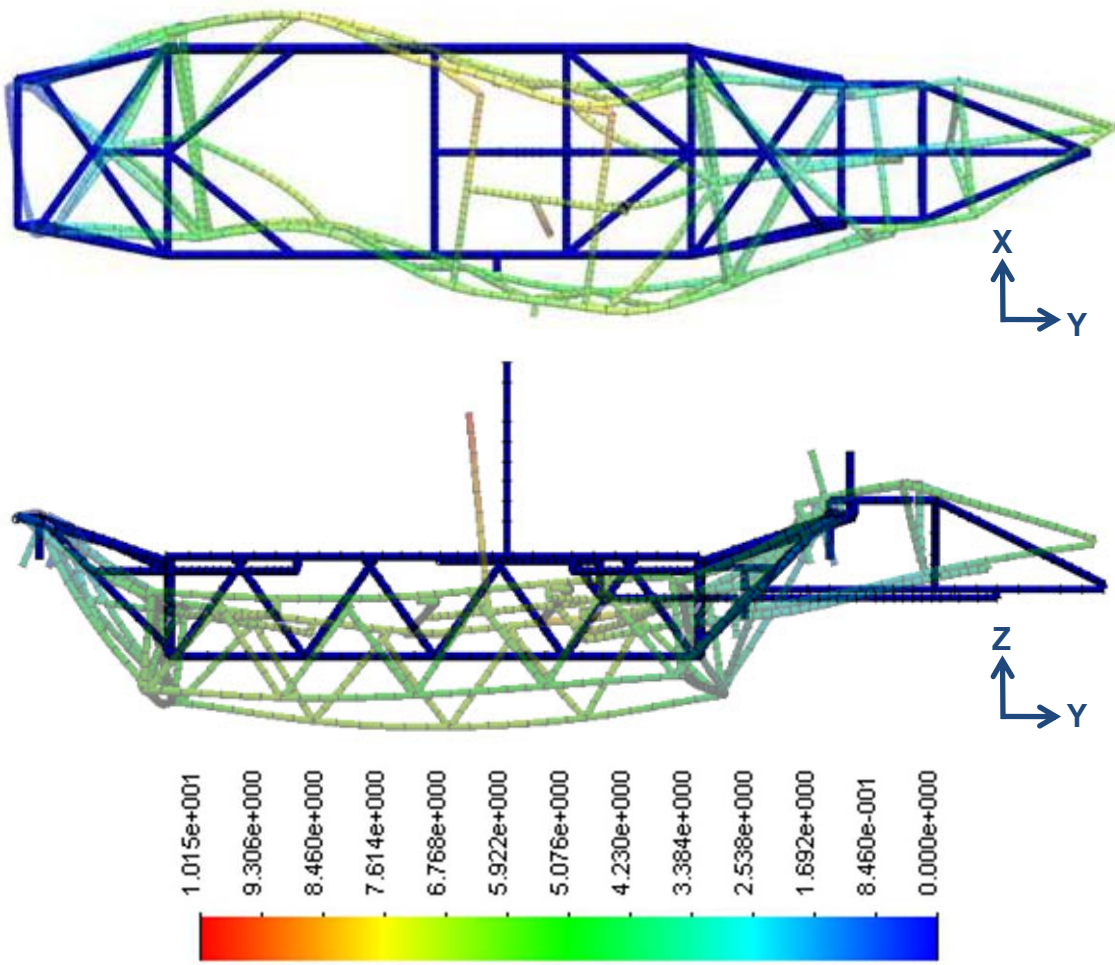


Figure 5.4: Overhead and side views of the second mode frequency response (units = mm, deformation scale = 125)

The third mode, 13.70 Hz, is also a heave mode but is limited almost entirely to the Y-drive and, to a lesser extent, the UX end of the bridge, Figure 5.5. The very tip of the Y-drive has the most travel, 17.55 mm [0.69 in.], which follows an arc in the Y-Z

plane. This movement causes significant translation of the payload along the Y-axis due to the fixed length of the screw. If the Y-drive support structure is attached to the bridge at a point further down the bridge then the amplitude of this heave mode could possibly reduce. This could increase the frequency at which this vibration occurs. To achieve this, the support structure would have to follow the angled path of the bridge beams tying the UX end to the main trusses or extend out over the X-bracing creating additional obscuration. For reference, the maximum deflection occurring in the primary beam is 7.40 mm [0.29 in.] and 9.19 mm [0.36 in.] in the secondary beam.

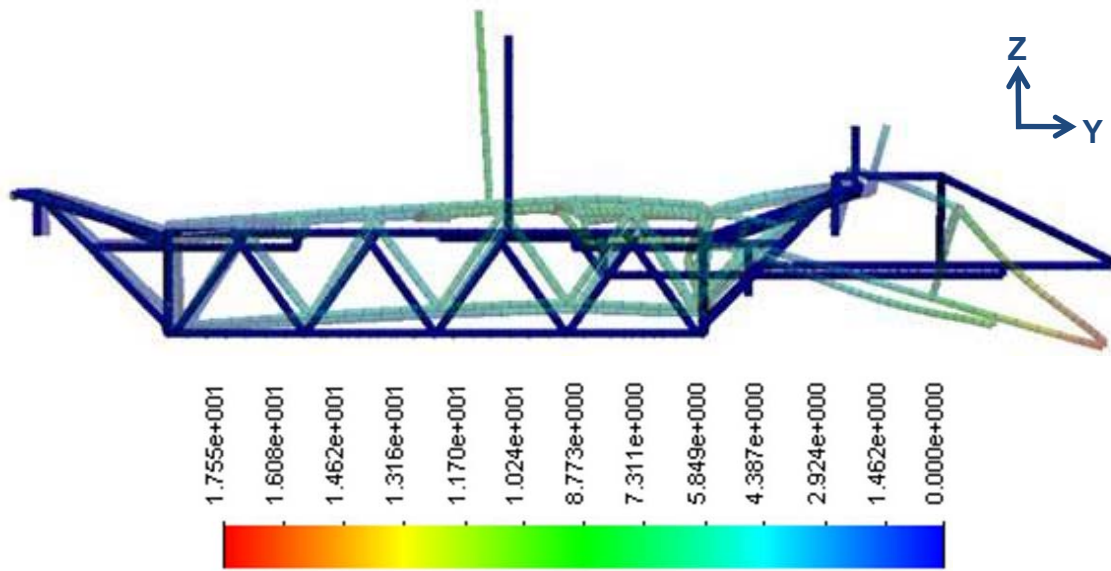


Figure 5.5: Side view of the third mode frequency response (units = mm, deformation scale = 55)

5.2. DEFLECTION ANALYSIS

A separate, static analysis is performed to measure the deflection in the main bridge beams. The only difference between this model and the frequency model is the inclusion of a gravity vector. This vector is positioned 35 degrees from the Z-axis in the

Y-Z plane. The HETDEX specification requires bridge deflection in the Z-axis under full payload be less than 2 mm with respect to deflection without the payload [27].

It became evident early in the design process that the frequency requirement is far more difficult to achieve than the deflection requirement. As a result, the deflection is only checked at major milestones in the design process, namely prior to design reviews and after major changes such as the inclusion of the center pull Y-drive.

Without the payload, the maximum self-weight deflection measured along the Z-axis is 0.751 mm [0.030 in.]. With the payload's CG positioned directly above the midpoint of the main bridge beams, the bridge measured 2.257 mm [0.089 in.] of deflection in the Z-axis. The resulting deflection caused by the 9044 kg payload is therefore the difference between these two measurements, 1.506 mm [0.059 in.]. The location of the greatest deflection is on the secondary beam near the joint with the lower cross member of the LHF as shown in Figure 5.6. For comparison, the much lighter HET bridge reportedly has 0.991 mm [0.039 in.] of deflection [28].

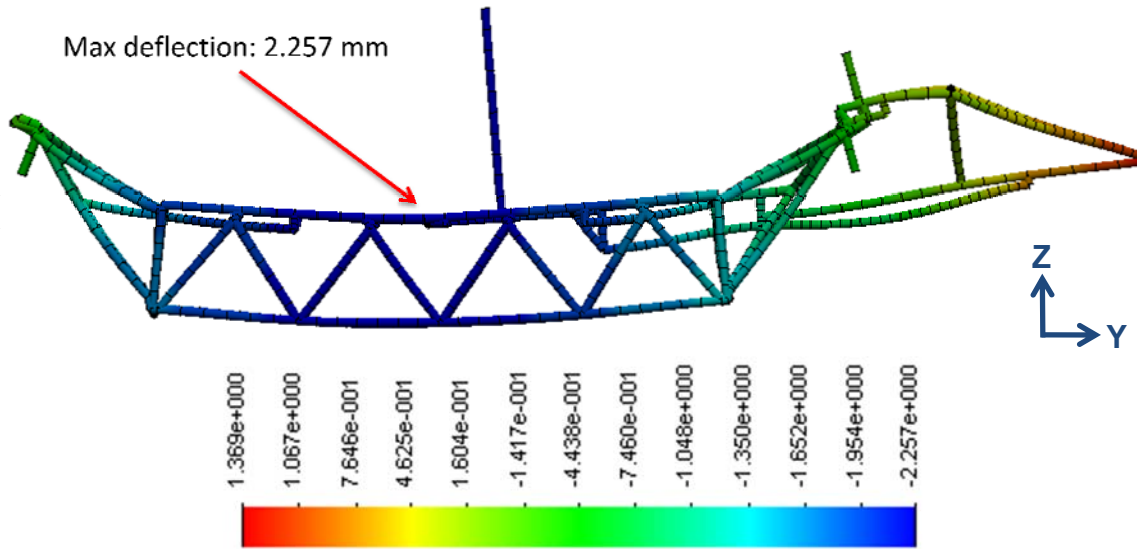


Figure 5.6: Bridge Z-axis deflection with the full payload resulting in maximum deflection of -2.257 mm (units = mm, deformation scale = 300)

5.3. STRESS ANALYSIS

Stress and buckling analyses are also performed on the bridge to ensure all beam members are within acceptable safety limits. A minimum safety factor of 2.0 to yielding was established as a design rule for each member. The gravity vector is applied in both analyses providing the only source of loading to the bridge. The same constraints used in the deflection and frequency analyses are applied.

SolidWorks Simulation provides four choices for viewing stress results: axial stresses, bending stresses in either of two orthogonal axes, and worst case stresses. Figure 5.7 displays the forces and moments applied to each end of every beam segment within the model [53]. These consist of an axial force, P, and two moments, M₁ and M₂. The worst case stresses are calculated by combining axial and bending stresses caused by M₁ and M₂ at a critical point on the cross-section and is the recommended stress to view

[53]. Viewing the axial stresses (force/area) reveals whether each beam is in tension or compression and its respective magnitude.

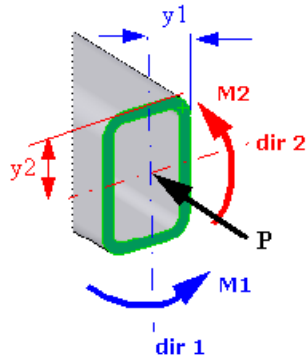


Figure 5.7: Beam segment loading convention applied in SolidWorks Simulation

Source [53]

Simulation uses a linearized buckling analysis to solve an eigenvalue problem to determine the critical buckling factors and the corresponding buckling mode shapes [53]. The critical buckling factor is the value when multiplied by a given beam's calculated axial load that buckling is estimated to occur. If this value is less than 1, then buckling is predicted to occur. Table 5.2 summarizes the meaning of the possible buckling load factors calculated by Simulation. The buckling mode shape is a visual representation of how the beam will buckle. This information can be helpful in modifying the beam geometry or support structure surrounding the beam to prevent buckling.

Table 5.2: Interpretation of possible buckling load factor (BLF) values

BLF Value (factor of safety)	Buckling Status	Notes
$1 < \text{BLF}$	Buckling not predicted	The applied loads are less than the estimated critical loads. Buckling is not expected.
$0 < \text{BLF} < 1$	Buckling predicted	The applied loads exceed the estimated critical loads. Buckling is expected.
$\text{BLF} = 1$	Buckling predicted	The applied loads are exactly equal to the estimated critical loads. Buckling is expected.
$\text{BLF} = -1$	Buckling not predicted	The buckling occurs when the directions of the applied loads are all reversed. For example, if a bar is under tensile load, the BLF should be negative. The bar will never buckle.
$-1 < \text{BLF} < 0$	Buckling not predicted	Buckling is predicted if you reverse all loads.
$\text{BLF} < -1$	Buckling not predicted	Buckling is not expected even if you reverse all loads.

Source [53]

5.3.1. Stress Results

Worst case stresses for the bridge are shown in Figure 5.8. The deformation scale is set at one and the color scale ranges from 0 MPa (blue) to 60 MPa [~ 8700 psi] (red). The results show that beams with the highest stresses are in the LHF and the screw mount extending from the LHF. Given the drastic simplifications made to these LHF members, these stresses can be neglected and are studied in a separate analysis using the actual LHF geometry.

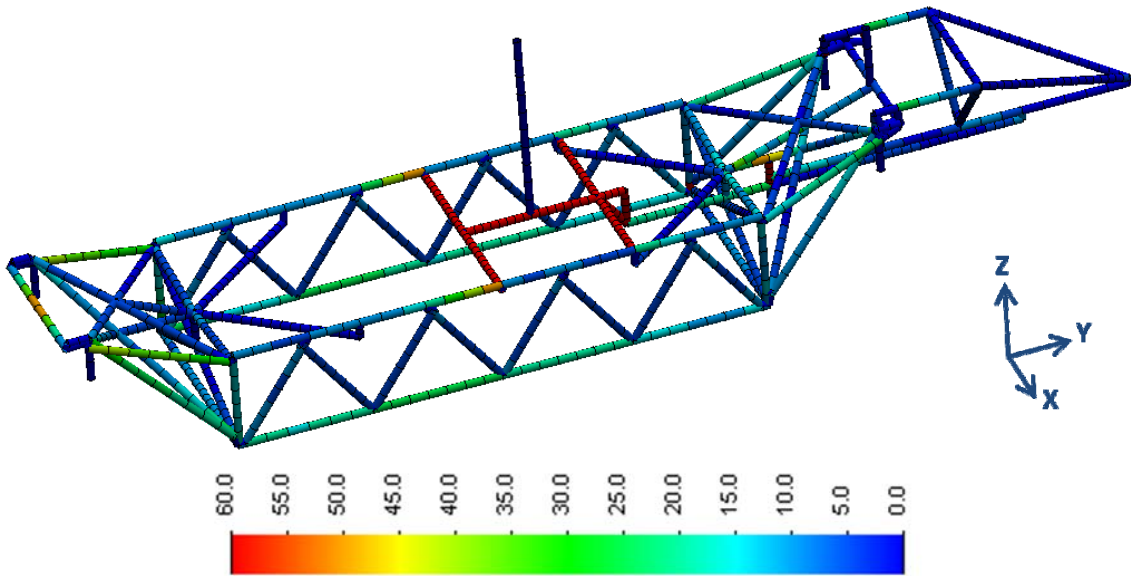


Figure 5.8: Results displaying the worst case stresses (units = MPa)

Ignoring the LHF beams reveals a few areas that share the maximum stress. The center of the LX end of the bridge at the skew bearing joint measures approximately 48 MPa [7000 psi] (shown as orange). The joints on the primary and secondary main beams of the bridge where the lower member of the LFH connects are two other areas with approximately 48 MPa stress. In all three of these locations, the beams in question have a factor of safety with respect to yielding greater than 5.

Figure 5.9 shows the axial stresses only in the bridge. Since the magnitudes of the stresses are all well within acceptable material limits, the color scale is modified to ± 0.01 MPa. This provides a simplified plot displaying beams in tension of any magnitude as red and beams in compression as blue. Green beams experience no axial stress due to the model's constraints or are beams that do not actually exist but are used to overcome modeling limitations. Given the manner in which the bridge deflects under

the weight of the payload, beams along the upper side of the bridge (referencing the Z-axis) are in compression while beams running along the lower side of the bridge are in tension. Analyzing this plot is a good check to ensure that the individual beam members are responding in the manner expected and that there is not a potential source of error built into the analysis.

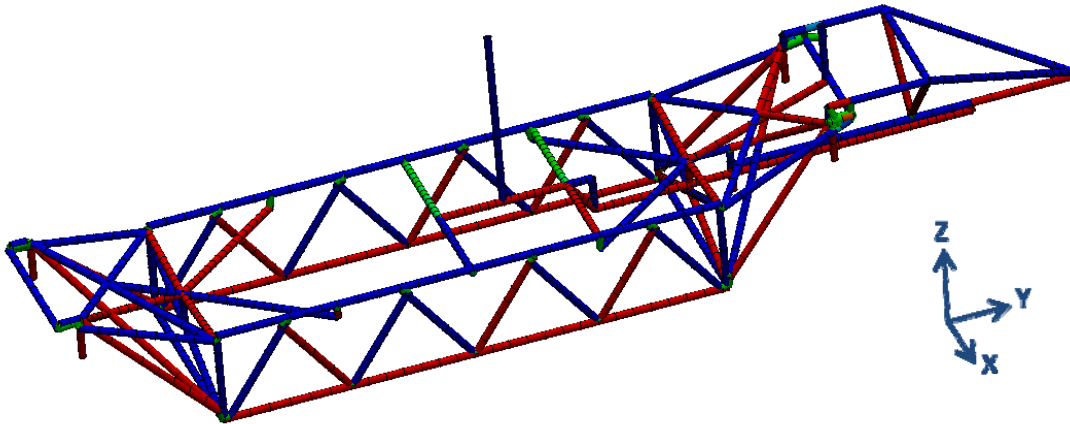


Figure 5.9: Plot showing each bridge beam in tension (red), compression (blue) or under no axial stress (green)

5.3.2. Buckling Results

Despite the relatively low axial stresses within the model, a buckling analysis is performed as a safety check due to the use of many long, slender bars and plates. Once again, the constraints of this analysis are identical to those of the other analyses performed and the gravity vector provides the only source of loading to the model.

Figure 5.10 displays the resulting plot for the first mode of the buckling analysis. The results show that the weakest beam with respect to buckling is the 1x9 in. lower runner from the primary truss to the LX bridge end. The stress analysis reveals that this member experiences an axial stress of 11.2 MPa [1625 psi] resulting in an axial tensile

load of ~65 kN [14,625 lbf]. The calculated buckling load factor is -7.61. Referring to Table 5.2, this means that the axial load would have to reverse (i.e. become a compressive load) and increase in magnitude by a factor of 7.61 (~495 kN) before this beam would buckle. The buckling mode shape predicts that this beam would bow outwards away from the bridge prior to buckling.

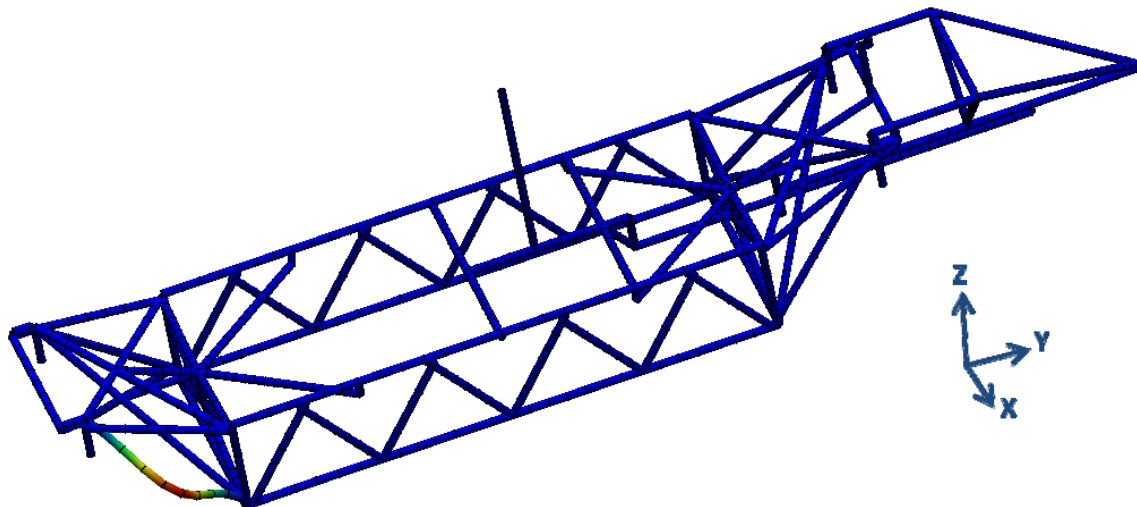


Figure 5.10: First buckling mode revealing the beam member most susceptible to buckling with a calculated buckling load factor of -7.61

While the first mode is generally the only mode of interest as it reveals the weakest beam in the structure, the next two modes are also examined. The matching runner on the secondary side of the bridge is the second mode with an identical mode shape to the first mode and a critical buckling factor of -8.05. The third mode returns to the same beam from the first mode but displays a different mode shape. This mode deforms the beam into an “S” shape and has a much higher critical buckling factor of -15.56.

From the buckling analysis, it is concluded that buckling should not be an issue on the bridge for the beams in use. The analysis assumes the ends of every beam are completely bonded, with the exception of the LHF members which have the standard beam releases to reflect the bearing arrangement. A far more likely failure mode to occur than buckling would be a poor weld joint failing at the end of a beam. This type of failure is completely preventable based on the quality of fabrication which will be discussed in the next chapter.

6. Fabrication

Good designs are always developed with fabrication processes and limitations in mind. Throughout the design process for the bridge, the team regularly discussed manufacturing limitations. One area of frequent discussion is the final machining processes required to mount hardware such as the Y-axis linear bearing rails and the manner in which the bridge will interface the upper hex.

The final bridge design is a collection of thin wall HSS tubing, solid bar stock and plates. All tubing is specified as ASTM A500, GR A while bar stock is designated to be ASTM A36 hot rolled structural steel due to its widespread use in many form factors, excellent weldability and good machining properties⁸ [54].

A brief overview of the fabrication process is as follows. The stock material shapes are laser cut to size, many beams requiring angled, if not compound angled, cuts. Once all of the parts are prepared, welding on the subassemblies begins. The bridge is constructed of six main subassemblies: the two main trusses, the two bulkheads and the two end assemblies. The bulkheads tie the main trusses together and then numerous pieces tie the bridge ends to the trusses including the X-braces and the side runners. Both

⁸ ASTM A36 has a machinability rating of 72 percent using ASTM 1212 as the standard of 100 percent

the upper and lower side runners are some of the more complicated parts to originally cut due to the compound angles involved.

Rectangular bar stock is welded to the bridge in areas where linear bearing rails are mounted. This stock material is later machined with the required mounting features for the rails. Additional items that weld onto the bridge are the two upper and two lower hard stops providing absolute limits for Y-travel, the four anti-skew pads which engage the upper hex to limit skewing and the mounting bracket for the Y-drive assembly.

6.1. WELDING SPECIFICATIONS

All thin-wall HSS tubing is joined with full penetration welds utilizing the preferred welding process dependent upon the joint (e.g. gas metal arc welding, shielded metal arc welding, etc.). All welds must adhere to AWS D1.1:2008 standards [55]. Plates and bar stock are welded with an assortment of fillet and groove welds as outlined in the drawing package initially prepared by CEM mechanical designer Dave Prater. Welds are accepted based upon the criteria for dye penetrant or magnetic particle inspection per AWS D1.1.

Individual subassemblies are thermally stress relieved per SAE AMS 2759/11 [56] during the fabrication process. Upon completion of all welding processes, the entire bridge will be thermally stress relieved. This step is deemed of particular importance due to the amount of post-machining and tight tolerances required in the final component. Neglecting to stress relieve the bridge could result in parts deforming during the machining processes or could lead to the formation of cracks within the welds.

6.2. MACHINING DETAILS

Several key machining operations are required on the bridge. The first areas are the ends of the bridge which are mounted to the upper hex bearing stacks. The section of the ends which bolt to the bearing mount plate is machined to a flatness of 0.1 mm [0.004 in]. The equivalent surface on the other end of the bridge is held coplanar to the first surface within 0.1 mm. This is a demanding tolerance given the nearly 10.4 meters of distance between these two surfaces. It is expected that shims will still be required during final assembly to correct tolerance stack-ups between the two ends of the bridge. These two areas become datum surfaces which other machined surfaces are referenced.

The second key area is maintaining parallelism between the three pairs of linear bearing rails. Per THK's mounting recommendations [51], a datum shoulder needs to be machined into the bar stock for the full length of the rail (6385 mm). A second shoulder is machined which will have tapped holes drilled every 600 mm. Bolts are used to press the rail against the datum shoulder before tightening the fasteners that hold the rail to the way. These features exist for both Y-axis rails. The primary rail way surface specifies a parallelism within 0.25 mm [0.010 in] to the mounting surface under the LX end of the bridge. The secondary rail surface has an additional callout to not only maintain that parallelism with the end of the bridge but also to the primary rail way by the same tolerance. The primary rail datum shoulder is required to be perpendicular to its way surface within 0.25 mm. The secondary rail datum is specified to be parallel to the primary rail datum within 0.10 mm. Due to the relaxed tolerances for the FMS rails, only a datum shoulder exists for these four rails. The geometric tolerances for these rails

d dictate that the datum shoulders will be parallel to the primary rail way within 0.5 mm [0.020 in].

An interesting method was proposed for machining the rail ways [57]. Few milling machines have the horizontal reach to machine both of the main bearing rail ways in one setup. As an alternative, the machinists will utilize a laser tracking system manufactured by Automated Precision Inc. [58]. The laser head unit remains stationary while the target is located at various locations along the ways. The laser maps these discrete points in 3D space using traceable metrology software called SpatialAnalyzer [59].

The mapping of the bearing way surface occurs with the bridge mounted horizontally, allowing the main beams to sag under their self-weight. Temporary bracing is put into place between the two main bridge beams before turning the bridge onto its side, preventing the beams from sagging along the X-axis (referencing tracker coordinates). The main beams are then deformed in the Z-axis in a manner to match that of the self-weight deflection when the bridge was horizontal. Using the vertical travel of the mill, both of the bearing ways are machined flat. When the bridge is set back upright, the ways will be flat despite the self-weight deflection.

The Y-axis linear encoder used to control the precise positioning of the payload is mounted to the same bar stock as the primary bearing rail. The mounting surface has a flatness requirement of 0.05 mm [0.002 in] and a parallelism callout of 0.25 mm referenced to the primary bearing rail datum. The surface also has a linear bolt hole pattern to mount the encoder.

The third area of machining is the mounting surfaces for the Y-drive. For optimal roller screw performance and life, radial loads transmitted through the nut are not desired [60]. Great care has therefore been given to ensure proper alignment between the roller screw axis and the Y-axis bearing rails. The two landing surfaces on the bridge for the Y-drive reinforcement are located on the upper bulkhead, Figure 6.1. The horizontal surface is to be machined parallel to the primary linear bearing rail way within 0.1 mm and the vertical surface is to be perpendicular to the same datum within 0.1 mm. Multiple adjustment features are also designed into the slew drive housing and the fixed and floating ends of the screw mounts to aid in alignment.

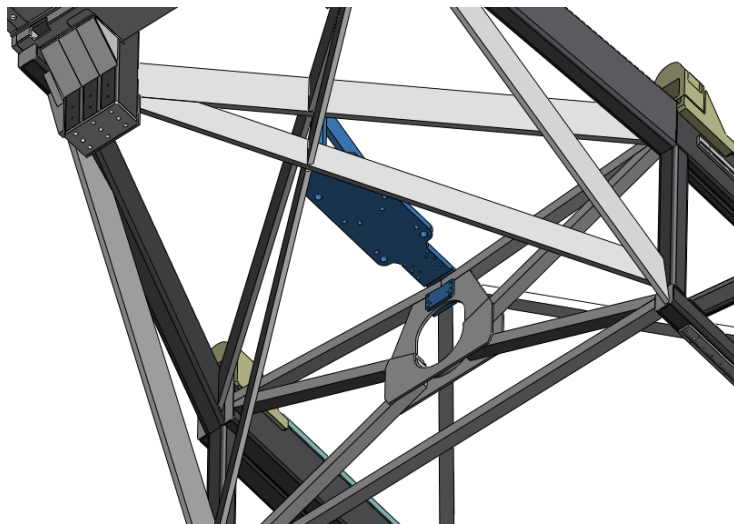


Figure 6.1: Machined mounting surfaces (shown in blue) for the Y-drive assembly

7. Discussion

The objective of this thesis is to present the design and analysis of the tracker bridge for HETDEX. Much of the exterior geometry of the bridge was dictated by the travel requirements and the hardware which the bridge must support. In addition to providing methods in which to support this hardware, the principle design effort created a very stiff but relatively lightweight structure. This is done while attempting to provide cost effective fabrication, limiting deflections and mass, and with the unusual requirement of minimizing the structure's cross-sectional area when viewed from above (to prevent light obscuration).

Finite element analyses are performed on the bridge to study the natural frequency response, deflection, stresses and buckling. All of these analyses utilize the exact same solid model and beam mesh within SolidWorks Simulation. The results produced by these studies, primarily the frequency response, allow the bridge design to be iteratively refined while optimizing the trade-off between stiffness and mass. A vast collection of modeling techniques are used in the analyses which include using lumped masses to represent subassemblies, modifying the modulus of elasticity of specific beam members, and modeling DOF through the use of constraints and beam releases. While the analyses still have known assumptions, it is as accurate a representation of the real bridge as could be modeled.

7.1. SUMMARY AND CONCLUSIONS

The tracker bridge for HETDEX was successfully designed and modeled utilizing 3D CAD software. The bridge design evolved as requirements changed and in response to the design of many subsystems which the bridge supports. Key changes in requirements, namely the relocation of the Y-drive, increased emphasis on reducing obscuration, and the addition of the CFD, lengthened the design process but also have led to a very functional final product. The tight coupling between SolidWorks and Simulation greatly sped the iterative process between making changes to the design and then quickly analyzing the impact of those changes.

The final first mode natural frequency of the bridge, 9.4 Hz, did not meet the original design goal of 10 Hz. It was known that this would be a difficult task given the vast increase in payload, but the current payload total is significantly greater than initial estimates (a factor of nearly 7 fold compared to the initial estimate of 4). Despite not being able to meet the stiffness requirement, MDO approved the design. The final bridge design did exceed the deflection requirement, 1.5 mm deflection out of the allowable 2.0 mm, and the amount of light obscuration was also deemed acceptable. While the total mass is greater than desired, it appears that the linear bearings will be able to theoretically support the load for the 20 year life cycle.

An interesting figure was presented by the HET design team concerning the original bridge design: the combined mass of the Y Beam (previous nomenclature for the bridge) and carriage (renamed the LHF for HETDEX) assemblies accounts for 68 percent of the total tracker's mass [28]. For HETDEX, only 52 percent of the total mass consists

of the bridge and LHF. While the published stiffness of the HET tracker is higher than HETDEX (11.53 Hz [28]), a significantly greater percentage of the tracker’s mass was devoted to obtaining this stiffness. Using a similar percentage with the greater HETDEX payload would result in a heavier tracker requiring substantially higher capacity bearings. As it stands, the entire HETDEX tracker has a mass greater than five times that of the HET tracker.

Material selection for the bridge was very straightforward and will utilize ASTM A36 for all bar stock and ASTM A500 for the tubing. These materials have more than adequate strength and will provide excellent quality welded joints. In the areas requiring post-machining, the material will not pose any unique challenges. The machining techniques planned for the bridge, on the other hand, are the first time that any of the engineers on the HETDEX team have encountered the use of a laser tracking system to aid in the machining process. According to Dave Weber, owner of Machine Works, the laser tracker and SpatialAnalyzer has completely changed the manner in which he operates his machine shop [57]. The past three years of using the laser tracker has revolutionized machining which had been nearly constant over his 30 year career. The introduction of CNC machine tools boosted productivity but the laser tracker can identify areas of potential trouble, such as self-weight deflection, which allows the machinist to address the issue on the front end instead of after the cuts have been made.

7.2. CONTRIBUTIONS

The major contributions of this thesis are listed below:

Development of the HETDEX Bridge – A computer solid model and a complete set of engineering drawings was created for the bridge which is currently undergoing fabrication. The functions and constraints for the design are described in Chapter 3 and the development of the model is described in Chapter 4. While two other similar bridges are currently in operation, each supports a science payload a fraction of the mass as HETDEX. The HETDEX custom corrector optics will allow astronomers to conduct the largest survey of galaxies ever performed, hopefully leading to revolutionary scientific breakthroughs concerning dark energy. This is only possible if the tracker can accurately position the instruments – a task dependent upon the bridge which supports all other subsystems.

Analysis of the HETDEX Bridge – The bridge is analyzed to meet design requirements for frequency response and deflection (see Chapter 5). The work performed applies a conventional theory (Euler-Bernoulli) and analysis techniques (software-driven FEA) to a specific design. Based upon research conducted, existing literature appears to lack examples of complex beam structure frequency responses, which this thesis addresses. Designers of large structures where stiffness is the primary design driver may be particularly interested in the bridge analysis for two reasons: 1) the design serves as a working example of the application of the beam theory to a complex structure; 2) it displays modeling techniques useful for creating a detailed FEA model.

Furthermore, this thesis details steps taken to maximize frequency response while limiting mass. Having greater experience in analyzing vibrations and interpreting frequency animations would have proven very helpful in this aspect of the design.

Perhaps only of interest to the field of astronomy, the manner in which beam form factors were manipulated to reduce obscuration while maintaining near-equivalent stiffness in specific planes has also been demonstrated. These techniques are essential in the field of astronomy when designing telescope components that must disrupt the light path between a target celestial object and the primary mirror. As obscuration increases, the telescope must remain focused on that object for a longer period of time to collect the required photons for analysis, lengthening tracking time. As has been overheard at MDO, it would be a shame for those photons to travel billions of light years to simply be reflected off of an object just meters away from the primary mirror. This technique may serve as an example to other niche applications desiring to minimize surface area in a particular plane for other reasons (e.g. reduce wind loading, drag, etc.).

7.3. FUTURE WORK

Upon completion of the bridge fabrication, it will be installed on a full size test stand at CEM mimicking the upper hex. The drive systems, hexapod and test masses representing the WFC and PFIP will all be installed on this test stand to identify any issues with the hardware and new control systems prior to installing the new tracker at MDO. This extensive testing exercise should drastically reduce the time required for final installation, minimizing down time on the telescope. When the entire tracker is installed on the telescope, it is desired to conduct natural frequency tests to experimentally determine the true resonant frequencies of the bridge. Only then can the accuracy of the bridge analysis be determined. While the corresponding mode shapes

will not be known, obtaining this data could potentially aid MDO engineers in future troubleshooting exercises.

When this data has been collected, the solid model can be revisited and modified if necessary to more closely match the measured response. Masses of the actual hardware can be recorded as parts are assembled which could be transferred to the model creating an as-built replica of the actual tracker. Once again, keeping this model as accurate as possible has potential benefits for MDO engineers to study the impact of future upgrades.

Another avenue to pursue would involve repeating the model validation for a final comparison to SolidWorks Simulation results. This repeated verification will aid in building confidence in the results produced by Simulation or, at the very least, bracket the results. Given the many changes made to the model since the first validation, this would require significant effort and it is not currently known whether such a process will be undertaken.

Issues were encountered with both SolidWorks and Simulation, more so than what has been discussed in this thesis. The weldment tool within SolidWorks has room for continued improvement. In particular, the trim/extend command used to eliminate overlapping beam material at joints currently has very limited capabilities. This is particularly true when making the compound trims needed in the bridge design. Furthermore, while the weldment tool has the ability to automatically join beams with mitered joints, Simulation prevents this feature from being used during an analysis. As a result, the user must choose whether the model will be used for design and graphical

purposes or for analysis and make selections accordingly. It would be very convenient if Simulation could automatically turn off the features that cannot be used in an analysis to prevent the dual modeling requirements.

Appendix A: Modeling Simplifications

The goal of FEA is to study the bridge beams and not the details of the subassemblies mounted to the bridge. The actual detailed models of the subassemblies are therefore replaced with simplified geometry to solely account for mass and the components' CG.

The payload is modeled as a hollow cylinder. The length of the cylinder, 2470 mm, is twice the height of the real payload's calculated CG to position the modeled payload's CG correctly. While the calculated CG is fairly accurate, continuing design effort on various components on the payload may have a minor effect on its correct location. An outside diameter of 1000 mm was arbitrarily chosen for the payload and the inside diameter was calculated to match the payload's mass of 9044 kg, using the density of A36 steel as the material.

Representing the Y-drive is somewhat more complicated. To ensure an accurate predicted frequency response, representing the approximate stiffness within the Y-drive is important. While the overall length is easy to duplicate, the complexity of the various components is simplified to model as beam elements. The Y-drive subassembly, including the roller screw, has a mass of 913 kg and is represented by 926 kg of hardware in the analysis model due to the simplifications. More important than the mass is the location of the subassembly's CG and stiffness characteristics. The modeled Y-drive's CG is located within 2 percent of the real model but matching the stiffness is much harder to control due to the limitations of beam modeling. Figure A.1 shows a cross section

view comparison of the real Y-drive housing and the one modeled for the bridge analysis. The primary difference is the ten 6.35 mm [0.25 in.] thick stiffeners spaced 400 mm apart down the length of the housing. Beam modeling prevents the addition of non-continuous features along the length of the housing.

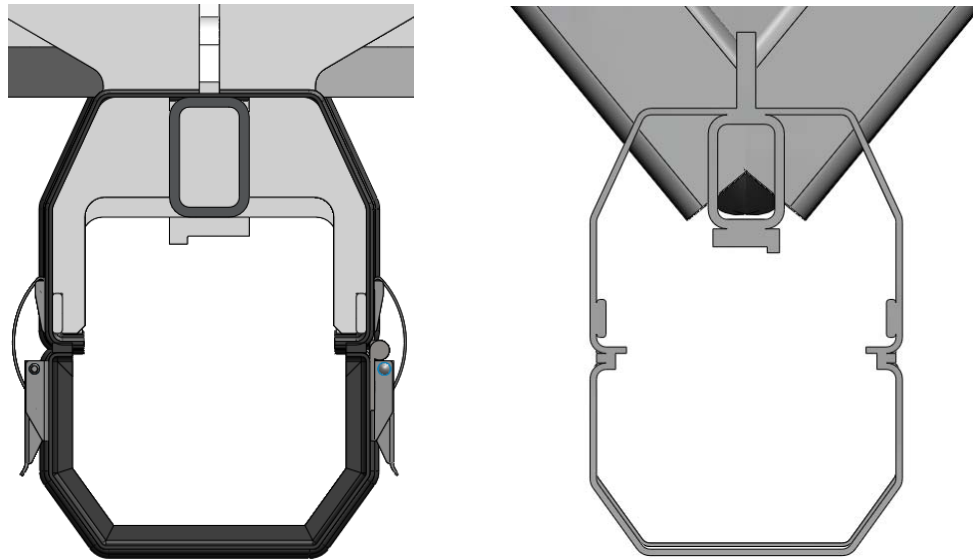


Figure A.1: Section view comparison of the real Y-drive housing model (left) and the model created for the beam analysis (right)

Source: CAD model created by HETDEX team

The “V-braces” are dropped 150 mm to align with the bottom surface of the main bridge beams to prevent an interference with the LHF. This creates a modeling issue as the software no longer recognizes a joint between the V-braces and main bridge beams due to the 150 mm offset between the beam centerlines. When meshing, the ends of the V-braces are left free. Short vertical beams are added to connect the free ends of the V-braces to the centerline of the main bridge beams. Since these short beams do not actually exist, the material properties are adjusted to make these beams artificially stiff. The modulus of elasticity is changed from 29.01E+6 to 29.01E+12 psi.

Likewise, the roller screw is modeled in its correct position along the Z-axis. The LHF has features to mount the fixed end of the roller screw, as previously described⁹. These $2 \times 2 \times \frac{3}{64}$ in. tubes are given the same Young's modulus as above to represent the actual, very stiff weldment. The CFD is modeled as a 400 mm diameter bar above the UX end of the bridge. The density of this round bar is modified so that the mass of the CFD, 584 kg, is correctly represented as well as the placement of its CG. The stiffness of this bar is also increased to prevent an artificial frequency mode from entering into the first three modes, being those of chief concern.

The Y-drive slew housing mounts beneath the upper X-braces. The slew housing contains the nut for the roller screw in addition to the slew motor and associated hardware. The slew drive bolts to the bridge from below and the nut is positioned at the center of the screw when the payload is located at mid-travel. The slew drive is modeled as a single $2 \times 2 \times \frac{1}{4}$ in. vertical beam. The Young's modulus is increased to represent the entire housing and the density is increased to correctly represent the actual slew drive assembly's mass of 178 kg. The nut acts as a retaining point for the long, flexible screw. The software creates a joint where the screw intersects the slew drive. The floating end of the screw is tied to the Y-drive housing with a short $2 \times 2 \times \frac{1}{4}$ in. tube whose end position is dependent on the location of the payload. This tube represents the screw's bearing housing and linear bearing block which allows the screw to translate.

⁹ Section 4.2.1, pg. 40

Additional point masses are added to the model in a few areas to further collaborate the analysis model to the detailed solid model. Just behind the UX and LX ends of the bridge are anti-skew blocks. These blocks, with a mass of 165 kg each, are hardware which makes contact with the upper hex in a full skewing condition. The hard stops defining the ends of travel for the LHF are located at the ends of the main beams. These are large machined blocks of steel with a mass of 50 kg each, designed to withstand an impact of the LHF at full slewing speed. Finally, the IFUs are guided by the FMS carriages which ride on the smaller pair of linear bearings on each side of the bridge. The mass of these carriages, in addition to the mass of the IFUs hanging below the bridge, is represented by point loads on the main bridge beams at the center of the LHF (305 kg per side).

Appendix B: Finite Element Analysis Constraints

A collection of bearings constrain the bridge to the upper hex. These bearings provide the bridge the necessary DOF and are similar to the bearing arrangement utilized on HET [28]. The UX end of the bridge has one additional DOF than the LX side to prevent the bridge from binding. Possibility of binding exists primarily because each end of the bridge is driven by a separate roller screw and drive system. While the tracker has a control system and precision linear encoders to ensure the tracker ends move uniformly, it is possible for one end of the bridge to lead or trail the other end. This condition is referred to as skew. The control system will shutdown if the linear encoders report too great a difference between the bridge ends and if that fails, proximity limit switches will kill power to the system if the bridge ends differ by more than 100 mm.

Another condition that exists due to the telescope architecture results from the bridge being mounted at a 35 degree angle. The LX bearings must react greater loads than the UX bearings. The Z-component of the bridge's mass is essentially uniform between the two rails but the Y-component is all reacted at the LX end.

Given the significant increase in bridge and payload mass for HETDEX, requiring the LX rail to react the entire Y-component load created two problems. The first is that even by upsizing the LX linear bearing from a 45 mm to a 65 mm rail, the blocks' predicted life falls well short of the required 20 year operational life and the static safety factor is less than two. In addition, John Good performed a frequency analysis of the entire telescope structure with the new bridge and payload and the first mode natural

frequency decreased to 4.39 Hz [61]. This value raised significant concern among HET engineers.

Good proposed a clever solution, further developed by CEM engineer Sarah Hinze, which allows the UX beam of the upper hex to react one-third of the Y-component weight. A collection of eight springs acting in parallel, named the spring pack, connects the bridge to the UX beam [62]. The springs are sized so that the effective spring rate supports one-third of the Y-component weight. The LX beam now only supports the remaining two-thirds of the weight. Despite introducing a source of compliance to the overall system, Good's analysis of the entire telescope predicts the overall first mode natural frequency increases to 5.12 Hz due to load sharing across the upper hex [61]. Welding a pair of MC12x31 in. channels to either side of the lower member of the upper hex adds additional stiffness and coupled with the spring pack raises the first mode to an estimated 5.35 Hz [61].

B.1. LX BEARING ARRANGEMENT

The primary DOF required by the bridge with respect to the upper hex is along the X-axis. A THK SHS65 linear bearing on the LX end and a THK SHS55 linear bearing on the UX end of the bridge provides this DOF. Due to the reduced loads on the UX end, a slightly smaller bearing can be used there.

On the LX end, the weight of the bridge is distributed to the linear bearing rail via four bearing blocks as shown in Figure B.1. The outer two X-blocks support the majority of the bridge's Z-component weight (shown as blue arrows in the figure). The inner two

X-blocks react the Y-component of the weight, seen both as a side load on the blocks (yellow arrows coming out of the page) and as a roll moment. The inner bearing stack supports only a small portion of the Z loading, essentially acting as a preload on the skew bearing. The final loading is from the drive system (red arrows) and is significantly minor in magnitude compared to the other two loads.

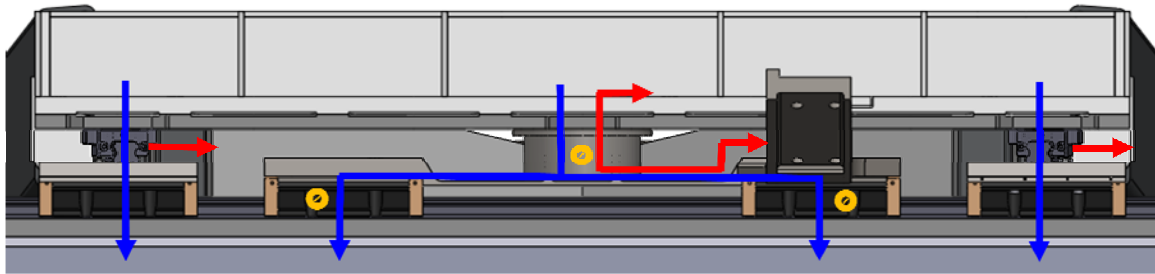


Figure B.1: End view of the LX end of the bridge showing the bearing arrangement and load paths where blue lines represent Z-axis loads, red lines are X-axis loads and yellow lines are Y-axis loads

The skew bearing, whose housing can be seen under the center of the bridge in Figure B.1, serves two functions: provides a central pivot point for the bridge during skew conditions and acts to transmit the Y-component of the weight to the X-axis linear bearing. Working in conjunction with the skew bearing, a pair of THK HCR45+22/800R bearings mount directly above the outer X-blocks at each corner of the bridge. The HCR bearings operate similarly as linear bearings with the exception that the rails are curved. Utilizing three separate bearings to provide the bridge a rotational DOF creates an important assembly condition that all three bearings must share a common point of rotation. This condition will be tightly controlled via tight machining tolerances on the mounting hole patterns for all three bearings.

The skew bearing itself is a double row cylindrical roller bearing (SKF PN: NN-3022-TN9-SP) mounted on a shaft with the outer housing bolted to the bearing mount plate. The shaft is part of the trolley which mounts to the inner two X-blocks and is the final part used to tie the bridge to the upper hex. The skew bearing has somewhat of a unique set of requirements for a rolling element bearing. The load acts radially against the bearing and is constant in its direction and while rotation is required, it is limited to only 0.54 degrees. Skew proximity switches limit the bridge to 0.54 degrees of rotation during operation (equating to 100 mm of linear X-travel between the bridge ends) and at 0.75 degrees of rotation metal-to-metal contact occurs between the bridge and the upper hex. This very limited amount of rotation means that individual rollers within the skew bearings are constantly loaded, and the loads are not evenly distributed between the rollers. Considerable analysis performed on the skew bearings with the help of SKF's engineering staff ensures the bearing chosen can operate successfully for the 20 year life span required.

The final source of loading for these bearings is the driving load from the screw. This load is transmitted through the trolley and is reacted by the center X-blocks as a pitch moment due to relative location of the nut to the blocks. The HCR bearings and skew bearing are loaded by this driving force as a side load, parallel to the X-axis (shown as red arrows).

Table B.1 displays the magnitudes of the loads supported by each bearing block on the LX end of the bridge. The loads are displayed per axis for each block in addition

to any moments being carried. These loads are then combined to determine the total equivalent load used to calculate static safety factors and theoretical life [51].

Table B.1: LX linear bearing loads per block

Load	Units	Corner Bearings		Trolley
		HCR45	SHS65	SHS65
X-axis	N	3000	0	0
Y-axis	N	0	0	35,415
Z-axis	N	16,467	32,933	5000
Moment	N-m	0	0	1718
Equivalent Load	N	19,467	32,933	98,814

B.2. UX BEARING ARRANGEMENT

The UX end has a very similar bearing arrangement with the addition of one DOF in the Y-direction, Figure B.2. The extra DOF is implemented with another set of linear bearing rails. Since the bridge is limited by hardware to 0.75 degrees of skew, only ± 0.5 mm of travel in the Y-direction is needed. The Y-axis linear bearings are therefore very short, providing 45 mm of travel for skew and to accommodate tolerance stack-ups during initial assembly. There are four Y-axis bearings used, two in the corners and two supporting the skew bearing in the center stack.

On the corners of the bridge, the Y-rails are sandwiched between the X-blocks and the HCR arced bearings. These bearings are subject to the same loading as the other bearings in these stacks, which are dominated by the Z-component of the tracker weight

(blue arrows) and also includes the driving load from the screw (red arrows parallel to the X-axis).

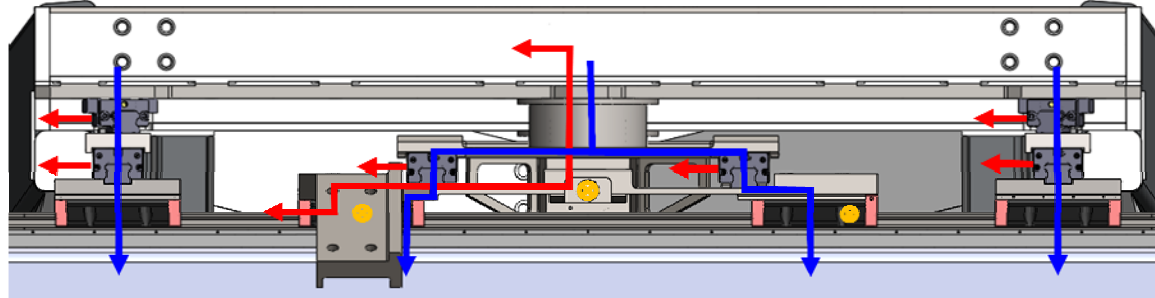


Figure B.2: End view of the UX end of the bridge showing the bearing arrangement and load paths where blue lines represent Z-axis loads, red lines are X-axis loads and yellow lines (into the page) are Y-axis loads

The center bearing stack on the UX end includes one additional part, the spring mount plate, located just below the skew bearing in Figure B.2. This plate has the skew bearing shaft welded to it and is bolted to the Y-blocks. In addition, the spring pack is mounted to the front section of this plate. A rod rigidly attached to the back half of the spring pack passes through a clearance hole in the spring mount plate and is threaded into the trolley. The front section of the spring mount plate reacts the load being supported by the spring pack.

The loads on the center bearing stack are similar to the LX end. A small Z-component load is supported by the center stack, creating a roll moment on the center pair of Y-blocks. The Y-blocks and skew bearing transmit the driving force to the bridge. The spring pack creates a force in the negative Y-direction which is reacted by the center X-blocks. These blocks transmit the load both as a side load and a roll moment. Magnitudes of loads carried in each axis for the bearing blocks are displayed in

Table B.2. The dominating loads driving the safety factor and life equations can clearly be seen for the various blocks.

Table B.2: UX linear bearing loads per block

Load	Units	Corner Bearings			Trolley Bearings	
		HCR45	SHS45	SHS65	SHS45	SHS65
X-axis	N	3000	3000	0	3000	0
Y-axis	N	0	0	0	0	19,372
Z-axis	N	16,467	32,933	32,933	5000	5000
Moment	N-m	0	0	0	338	531
Equivalent Load	N	19,467	35,933	32,933	23,840	45,727

B.3. LHF BEARING ARRANGEMENT

The final bearing arrangement set are the bearings holding the LHF to the bridge as designed by Ian Soukup [45]. The main bearings are a pair of THK SHS65 that extend the length of the bridge providing the main DOF along the Y-axis. One bearing rail is mounted to each of the main beams of the bridge. Four blocks, two per rail, support the LHF.

While the payload is not expected to skew due to the single, center-pull roller screw, an additional DOF in the X-axis is provided on the secondary bridge beam. This bearing configuration was used on the original bridge [28], and a similar arrangement is deployed to decouple the two Y-axis bearing rails. This is accomplished by mounting 246 mm long THK SHS55 linear bearing rails directly above the Y-blocks, Figure B.3.

This DOF will prevent the payload from binding if the two Y-rails have misalignment upon installation.

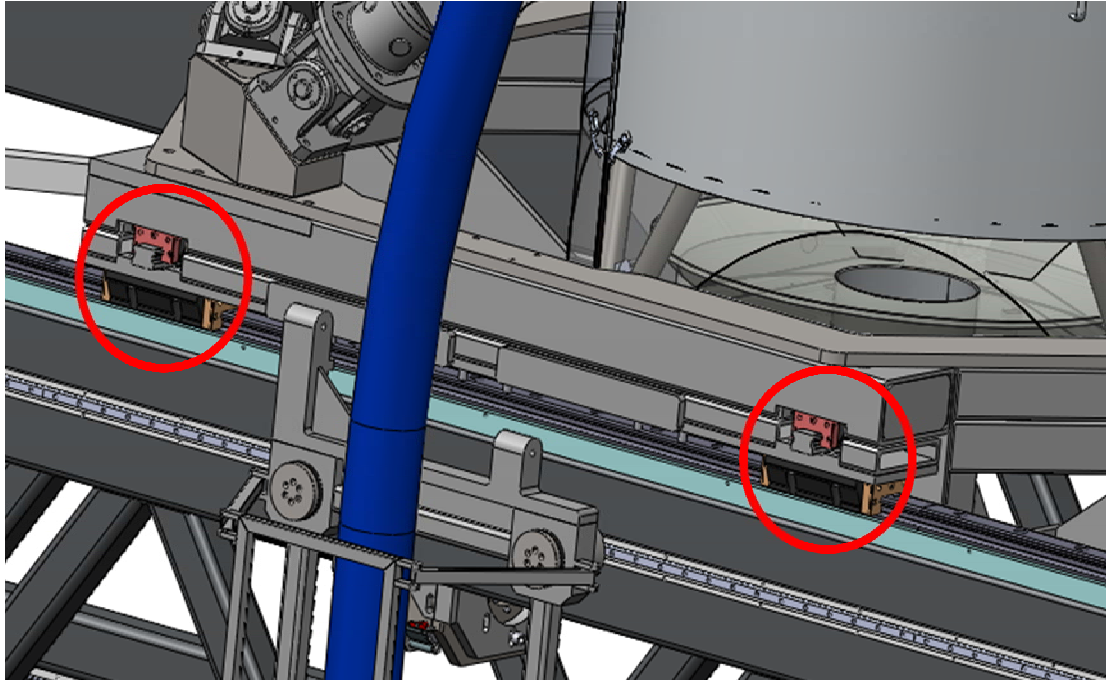


Figure B.3: View of the secondary side of the bridge revealing the X-blocks on short rails mounted directly above the main Y-blocks

Source: CAD model created by HETDEX team

To represent these bearings in the model, a different approach is utilized. Since the mock LHF is represented by beams within the model, standard Simulation constraints cannot be applied at the bearing locations. Instead, the ends of the beams are modified from their default rigid condition. SolidWorks allows the user to pick any individual beam and to apply DOF(s) to either end of the beam. For the case of the two members spanning the main bridge beams, the ends of the beams on the secondary rail of the bridge are freed in the X and Y axes representing the linear bearings. The beam ends on the primary rail are freed along the Y-axis.

Appendix C: Modeling Validation

SolidWorks first introduced beam meshes in their 2007 release of CosmosWorks (renamed Simulation for the 2009 release). Coincidentally, the bridge modeling process began while using the 2007 release. Not surprising given the complexity of the software, problems were encountered with the software given its short history with beam meshes. SolidWorks Corporation made significant changes to the beam meshing analysis in subsequent releases to an extent not common for mature software. Continued changes were made between the 2008 and 2009 releases. While changes to the graphical user interface are quickly recognized, the changes made to the code in how the software performs calculations are not as obvious.

As a result, good modeling practice suggests repeating an identical analysis in the new release as one that had just been performed in the previous release with the expectation of the results matching very closely. This was not the case when transitioning between the 2007 and 2008 releases. Due to a nearly 100% increase in frequency results, a detailed modeling verification took place to ensure that the results could be trusted.

To continue progressing with the bridge design, Dr. Brian Murphy at CEM was brought onto the project to work with John Good to perform an extensive modeling verification. Good recreated the bridge using Algor FEA software [63]. Beginning with simple models constructed with HSS thin walled tubes and eventually arriving at the full

bridge model, Good and Dr. Murphy ran independent analyses between software packages and compared results.

Presenting the comparison results to SolidWorks Corporation, it was determined that Simulation has a problem calculating the polar area and mass moments of inertia of non-circular cross-section beams. These errors are believed to be the source of the differences, in which Simulation repeatedly predicts frequency responses approximately 10 percent higher than Algor for the first mode of the bridge. Higher modes are within 2 percent of Algor's results, however in these cases Simulation predicts the lower value, Table C.1. Given the tight coupling between Simulation and SolidWorks, it was decided to continue utilizing the Simulation package but to always present results highlighting this issue.

Table C.1: Model validation results comparing Simulation and Algor

Freq. Modes [Hz]	1 st Mode	2 nd Mode	3 rd Mode	4 th Mode	5 th Mode
Simulation	8.61	9.66	14.63	15.08	16.09
Algor	7.78	9.75	14.78	15.32	15.34
% Difference	+9.6	-0.9	-1.0	-1.6	+4.7

Source: John Good (McDonald Observatory) and Dr. Brian Murphy (CEM) with results presented in [50]

One final issue that identified during the validation effort involves the correct wall thicknesses to use for HSS tubes. According to AISC [64], the proper wall thickness to assume for engineering calculations is 93 percent of nominal. This reduction in strength corresponds to the manufacturing tolerances allowed for ASTM A500 steel [65], which is

specified for the bridge. The thicknesses in all tubing profiles were reduced accordingly for use in all subsequent analyses.

References

- [1] University of Texas Department of Astronomy website, Hobby-Eberly Telescope, <<http://www.as.utexas.edu/mcdonald/het/het.html>> (October 10, 2009)
- [2] McDonald Observatory website, About McDonald Observatory, <<http://mcdonaldobservatory.org/news/facts/about.html>> (October 10, 2009)
- [3] Ramsey, L.W., et al., 1998, "The early performance and present status of the Hobby-Eberly Telescope," *Proc. SPIE* **3352**, p.34
- [4] Krabbendam, V.L., Sebring, T.A., Ray, F.B. & Fowler, J.R., 1998, "Development and performance of Hobby-Eberly Telescope 11-m segmented mirror," *Proc. SPIE* **3352**, 436
- [5] Hill, G.J., MacQueen, P.J., Ramsey, L.W., Shetrone, M.D., 2004, "Performance of the Hobby-Eberly telescope and facility instruments", *Proc. SPIE* **5492**, p. 94-107
- [6] Hobby-Eberly Telescope Dark Energy Experiment website, Homepage, <<http://hetdex.org>> (October 10, 2009)
- [7] Hill, G.J., et al., 2008, "The Hobby-Eberly Telescope Dark Energy Experiment (HETDEX): Description and Early Pilot Survey Results", *Astronomical Society of the Pacific Conference Series*, Vol. 399: Panoramic Views of Galaxy Formation and Evolution, p. 115
- [8] Savage, R.D., et al., 2010, "Current status of the Hobby-Eberly Telescope wide-field upgrade", *Proc. SPIE* **7733**, 149 (pending publication)
- [9] John M. Hill's WWW Home Page, Presently Operating Reflecting Telescopes, <<http://abell.as.arizona.edu/~hill/list/bigtel99.htm>> (November 9, 2009)
- [10] Han, S.M., Benaroya, H., Wei, T., 1999, "Dyanmics of Transversely Vibrating Beams Using Four Engineering Theories", *Journal of Sound and Vibration*, Vol. 225, Issue 5, p. 935-988
- [11] Lord Rayleigh, 1877, *Theory of Sound 2nd Ed.*, New York, NY: Macmillan
- [12] Timoshenko, S. P., 1921, "On the correction for shear of the differential equation for transverse vibrations of bars of uniform cross-section", *Philosophical Magazine*, p. 744
- [13] Timoshenko, S. P., 1922, "On the transverse vibrations of bars of uniform cross-section", *Philosophical Magazine*, p. 125
- [14] Vlasov, V.Z., 1961, "Thin-Walled Elastic Beams", *Israel Program for Scientific Translations*, 2nd Ed., Jerusalem
- [15] Ahmad, M.F., Guile, C.W., 1990, "Analysis of coupled natural frequencies of thin-walled beams with open cross sections using MSC/NASTRAN", *MSC 1990 World Users' Conference Proceedings*, #1590
- [16] Banerjee, J. R., 1999, "Explicit frequency equation and mode shapes of a cantilever beam coupled in bending and torsion," *Journal of Sound and Vibration*, Vol. 224, p. 267–281
- [17] Prokić, A., 2005, "On triply coupled vibrations of thin-walled beams with arbitrary cross-section," *Journal of Sound and Vibration*, Vol. 279, p. 723–737
- [18] Prokić, A., Lukić, D., 2007, "Dynamic behavior of braced thin-walled beams", *International Applied Mechanics*, Vol. 43, No. 11, p. 1290-1303
- [19] Bakker, M.C.M., Peköz, T., 2003, "The finite element method for thin-walled members – basic principles", *Thin-Walled Structures*, Vol. 41, p. 179-189
- [20] Sarawit, A.T., Kim, Y., Bakker, M.C.M., Peköz, T., 2003, "The finite element method for thin-walled members – applications", *Thin-Walled Structures*, Vol. 41, p. 191-206

- [21] Przemieniecki, J.S., 1968, *Theory of Matrix Structural Analysis*, New York, NY: McGraw-Hill
- [22] Buckley, D.A.H., Swart, G.P., Meiring, J.G., 2006, "Completion of the Southern African Large Telescope", *Proc. SPIE* **6267**, 0Z
- [23] Willem, S., et al., 2003, "Structural design of the Southern African Large Telescope", *Proc. SPIE*, **4837**, 272
- [24] Stobie, R., Meiring, J.G., Buckley, D.A., 2000, "Design of the Southern African Large Telescope (SALT)", *Proc. SPIE*, **4003**, 355
- [25] Personal interview, Joseph Zierer, Mechanical Engineer, Center for Electromechanics, March 5, 2010
- [26] Personal interview, Ian Soukup, Mechanical Engineer, Center for Electromechanics, March 1, 2010
- [27] Center for Electromechanics, "HETDEX Tracker and Fiber Management System Specification", CEM Document #RF272, Rev G (in progress), August 17, 2009
- [28] Booth, J. A., Ray, F. B., and Porter, D. S., 1998, "Development of a star tracker for the Hobby Eberly Telescope", *Proc. SPIE*, **3351**, 20
- [29] Booth, J.A., et al., 2006, "The Wide Field Upgrade for the Hobby-Eberly Telescope", *Proc. SPIE* **6267**, 97
- [30] Hill, G., et al., 2008, "Present and future instrumentation for the Hobby-Eberly Telescope", *Proc. SPIE* **7014**, 06
- [31] Hill, G.J., et al., 2008, "Design, construction, and performance of VIRUS-P: the prototype of a highly replicated integral-field spectrograph for HET", *Proc. SPIE* **7014**, 257
- [32] Savage, R.D., et al., 2008, "Current Status of the Hobby-Eberly Telescope Wide Field Upgrade and VIRUS", *Proc. SPIE* **7012**, 10
- [33] Hill, G.J., MacQueen, P.J., Ramsey, L.W. & Shetrone, M.D., 2004, "Performance of the Hobby-Eberly Telescope and Facility Instruments", *Proc. SPIE* **5492**, 94
- [34] Good, J.M., et al., 2008, "Current Status of the HETDEX Fiber Optic Support System", *Proc. SPIE* **7014**, 280
- [35] Radiation Systems, Inc., "Upper Hex Assy", Drawing Number 15805, Rev A, December 21, 1994
- [36] McDonald Observatory, "Hobby-Eberly Telescope Specifications", Internal Report, Report #JAB94-065, October 5, 1994
- [37] Personal interview, Hanshin Lee, Postdoc Student, McDonald Observatory, February 11, 2010
- [38] McDonald Observatory, "HET Operations Staff Requirements", Internal Report, January 14, 2008
- [39] Orbital Sciences Corporation, "Rotary Drive Mechanism", Drawing Number 1010-0012, Rev A
- [40] Orbital Sciences Corporation, "Y Beam Frame Assembly", Drawing Number 1010-0021, Rev D
- [41] Phone interview, Sarah Zyburt, Application Engineer, THK, May, 2008
- [42] Mollison, N.T., et al., 2010, "Design and development of a long-travel positioning actuator and tandem constant force actuator safety system for the Hobby-Eberly Telescope wide-field upgrade", *Proc. SPIE* **7733**, 150 (pending publication)
- [43] Zierer, J., "Hexapod, Strongback and PFIP Support Structure", Critical Design Review I Presentation, Center for Electromechanics, December 16, 2008

- [44] Zierer, J.Z., et al., 2010, "The development of high-precision hexapod actuators for the Hobby-Eberly Telescope Dark Energy Experiment (HETDEX)", *Proc. SPIE* **7733**, 49 (pending publication)
- [45] Soukup, I., "Carriage", Critical Design Review II Presentation, Center for Electromechanics, May 12, 2009
- [46] Phone interview, Leon Nel, Lead Design Engineer, Southern African Large Telescope, September 18, 2008
- [47] Personal interview, John Good, Mechanical Engineer, McDonald Observatory, November 7, 2009
- [48] Center for Electromechanics, "Mass Summary", Internal Report, Document #10221-ML-001, REV XB, November 13, 2009
- [49] SolidWorks website, Homepage, Dassault Systèmes SolidWorks Corporation, <<http://www.solidworks.com/default.htm>> (October 10, 2009)
- [50] Worthington, M., "Tracker Bridge", Critical Design Review I Presentation, Center for Electromechanics, December 16, 2008
- [51] THK Co., LTD., 2008, "General Catalog: Linear Motion Systems", Catalog No.500E
- [52] Worthington, M., "Tracker Bridge", Preliminary Design Review Presentation, Center for Electromechanics, May 29, 2008
- [53] Dassault Systèmes SolidWorks Corporation, "SolidWorks Simulation 2009 Online User's Guide", 2009
- [54] Earle M. Jorgensen Company, "Reference Book", Section D: Plates, 2007
- [55] AWS D1.1/D1.1M, 1972 (2008), "Structural Welding Code – Steel", American Welding Society, 2008, ISBN 978-0-87171-090-1
- [56] SAE AMS 2759/11, 2005, "Stress Relief of Steel Parts", SAE International, 2005
- [57] Personal interview, Dave Weber, Owner, Machine Works, October 2009
- [58] Automated Precision Inc. website, Homepage, <<http://www.apisensor.com/starten>> (November 18, 2009)
- [59] New River Kinematics website, Products, <<http://www.kinematics.com/products/index.html>> (November 22, 2009)
- [60] Phone interview, Ali Namous, Applications Engineer, SKF, May 2008
- [61] Good, J., "HET Structure Mode Improvement Study", HETDEX Internal Report, October 26, 2008
- [62] Worthington, M., "Tracker Bridge", Critical Design Review II Presentation, Center for Electromechanics, May 12, 2009
- [63] Algor website, Homepage, Autodesk, <<http://www.algor.com>> (November 9, 2009)
- [64] Stine, T.S., 2005, "Specifying HSS", *Modern Steel Construction*, July 2005
- [65] ASTM Standard A 500/A 500M, 1999 (2007), "Standard specification for cold-formed welded and seamless carbon steel structural tubing in rounds and shapes", ASTM International, West Conshohocken, PA, 2007, DOI: 10.1520/A0500_A0500M-09

Vita

Michael Scott Worthington was born in Dallas, TX. He grew up in Lafayette, LA and Anchorage, AK prior to graduating from Katy High School in Katy, TX. He received the degree of Bachelor of Science in Mechanical Engineering from Texas A&M University in May 2002. Michael began employment at the University of Texas' Center for Electromechanics in Austin, TX as a research engineer in May 2002. While continuing to work full time, he entered graduate school at the University of Texas in June 2006.

Permanent address: 1103 Debco Lane

Spicewood, TX 78669

This thesis was typed by the author.